Available online at www.sciencedirect.com
ScienceDirect
Comput. Methods Appl. Mech. Engrg. 339 (2018) 61–90
Computer methods in applied mechanics and engineering
www.elsevier.com/locate/cma

A new isogeometric topology optimization using moving morphable components based on R-functions and collocation schemes

Xianda Xie[a], Shuting Wang[a], Manman Xu[a], Yingjun Wang[b,*]

[a] School of Mechanical Science and Engineering, Huazhong University of Science and Technology, Wuhan, 430074, China
[b] National Engineering Research Center of Novel Equipment for Polymer Processing, The Key Laboratory of Polymer Processing Engineering of the Ministry of Education, School of Mechanical and Automotive Engineering, South China University of Technology, Guangzhou, 510641, China

Received 1 December 2017; received in revised form 23 March 2018; accepted 27 April 2018
Available online 9 May 2018

Abstract

This paper presents a new isogeometric topology optimization (TO) method based on moving morphable components (MMC), where the R-functions are used to represent the topology description functions (TDF) to overcome the C^1 discontinuity problem of the overlapping regions of components. Three new ersatz material models based on uniform, Gauss and Greville abscissae collocation schemes are used to represent both the Young's modulus of material and the density field based on the Heaviside values of collocation points. Three benchmark examples are tested to evaluate the proposed method, where the collocation schemes are compared as well as the difference between isogeometric analysis (IGA) and finite element method (FEM). The results show that the convergence rate using R-functions has been improved in a range of 17%–60% for different cases in both FEM and IGA frameworks, and the Greville collocation scheme outperforms the other two schemes in the MMC-based TO.

Keywords: Topology optimization; Moving morphable components; R-functions; IGA; Collocation schemes

1. Introduction

Aiming at finding the optimal material distribution in a design domain under certain constraints, topology optimization (TO) has been attracting more and more research attention since the pioneering work of Bendsøe and Kikuchi [1]. Many approaches have been proposed to solve TO problems in the past thirty years, such as homogenization method [1], solid isotropic material with penalization (SIMP) approach [2,3], level set method [4–9], and evolutionary approach [10]. TO has made a considerable progress by integrating with other physical disciplines and successfully applied to numerous industrial fields, such as aircraft [11–13], additive manufacturing [14–16] and design in photonics [17,18]. Recently, a remarkable work of Aage et al. [19] has been published in Nature for optimizing the design of the internal structure of a full-scale aeroplane wing.

* Corresponding author.
E-mail address: wangyj84@scut.edu.cn (Y. Wang).

https://doi.org/10.1016/j.cma.2018.04.048
0045-7825/

In TO, lacking for the explicit boundary geometric information in the final optimal results is one of the biggest barriers for the TO engineering application. In order to solve this problem, Guo et al. [20] innovatively proposed an explicit TO approach based on the concept of moving morphable components (MMC). The basic idea of this method originated from that arbitrary complicated topology can be decomposed into a finite number of components and the desired topology structure can be obtained by optimal component distribution having the optimized central position, length, inclined angles, and some other geometrical features of components [20]. An ersatz material model is proposed where Young's modulus is defined as the product of unit Young's modulus, the mean value of p-power of nodal Heaviside values denoted as the Young's modulus coefficient, as well as the density field is obtained from the mean value of nodal Heaviside values in [20]. MMC-based TO has been successfully applied to handle several types of topology problems such as minimum length scale control [21,22] and structural complexity control [23,24]. Recently, another type of explicit boundary TO based on moving morphable void (MMV) was presented for three dimensional TO problems [25], which has been applied to self-supporting structure design in additive manufacturing [16]. Compared to traditional structural TO approaches, the MMC-based and MMV-based TO frameworks can not only include explicit geometric information into the TO process, but also greatly reduce the number of design variables during the optimization process [26,27]. However, conventional MMC-based and MMV-based TOs are based on the finite element method (FEM) using linear finite elements, which result in some numerical problems in conventional MMC-based and MMV-based TOs. The first one is the numerical instabilities which may leads to instable result caused by the linear shape functions of finite element mesh [28]. The second one is the disconnection between analysis models and geometric models [29]. The third one is that computational cost will greatly increase when quadratic (or higher order) elements are used, e.g., the ratio of linear Lagrange quadrilateral elements to nodes is roughly one, but for quadratic elements, it increases to four [29]. Lastly, the linear finite elements may cause the instability of checkerboard pattern [30].

The numerical instabilities of the linear finite elements and high computation burden of quadratic (or higher order) finite elements in TO problems as mentioned above can be addressed by IGA due to its high accuracy and efficiency. The IGA is a relatively new method proposed by Hughes et al. [31], which represents partial differential equation (PDE) unknowns in the process of analysis with CAD mathematical primitives, e.g., B-spline or NURBS. Logically, IGA is an extension of the classical FEM. However, compared to FEM, IGA has many inspiring merits. Firstly, the accuracy per degree of freedom (DOF) can be improved by the smoothness of splines in IGA. Secondly, the PDEs of IGA can be efficiently solved without geometric approximation due to the use of NURBS basis function. Last but not least, the computational efficiency of high order elements is largely improved, e.g., the ratio between DOFs of FEM and that of IGA approaches to 4 for quadratic elements. With these advantages compared to traditional FEM, IGA is becoming more and more popular in the academic community [32]. Many researchers devote to using various new modeling techniques, such as T-splines [33,34], hierarchical B-Splines [35,36] in the IGA and apply it to the fluid, fluid–solid interaction [37,38], beams and shells [39–42], fracture [43] and many other mechanical analysis fields. The effectiveness of IGA has been verified by a variety of engineering problems [37,39,42,44–47].

Recently, as a replacement for FEM, IGA used in structural TO has received attention by researchers. With the use of trimmed spline surfaces, a method for isogeometric TO (ITO) is proposed by Seo et al. [48], while the computational time for the analysis may increase considerably when the number of trim curves in a trimmed surface is large. As pointed out by Dedè et al. [49], the capability of IGA that embeds the CAD geometric representation in the analysis and optimization provides higher accuracy and makes the design domain can be exactly modeled. Similarly, those advantages are elaborated in Ref. [49] where an ITO with a phase field model for both 2D and 3D problems is presented. To avoid shape irregularities such as "islanding" and "layering", Kumar et al. [50] use B-spline elements to obtain the shape boundaries, since B-spline elements are able to represent the density as tangent continuous and even curvature continuous functions so that the contours of shape boundaries (function of density) have similar continuity and smoothness. Wang et al. [29] proposes an accurate and efficient ITO by integrating IGA with parameterized level set method, and based on such ITO, Wang et al. [51] further take arbitrary geometric constraints into consideration to satisfy some practical requirements. Moreover, using the theory of asymptotic homogenization, an ITO scheme for lattice materials with either isotropic, or anisotropic is proposed by Wang et al. [46]. Very recently, Lieu et al. [52] presents a multi-resolution approach for the multi-material TO problem based on the IGA in which a new variable parameter space is added to define design variables and represents the optimal distribution of all material phases based on the bivariate B-spline basis functions.

Inheriting both the advantages of MMC-based TO and IGA, a novel approach of explicit ITO using MMC (ITO-MMC) is introduced by Hou et al. [28]. ITO-MMC is able to improve stability and robustness of the numerical

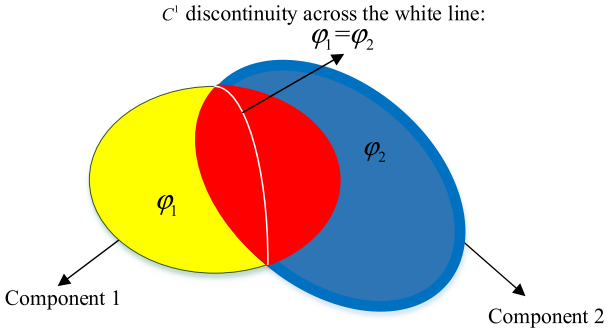

Fig. 1. The illustration of C^1 discontinuity of two MMCs.

performance over the conventional MMC-based TO due to the replacement of FEM by IGA. However, as depicted in Fig. 1, a common imperfection of both conventional MMC-based TO and ITO-MMC is that the C^1 discontinuity is introduced when the TDF values of points in the overlapping regions of MMCs are computed by max function as that in Refs. [20,21,27], so that the objective function is not differentiable in the structure which may lead to a low convergence rate of TO.

In computational geometry and object modeling, an arbitrary geometric shape in engineering can be represented by a function generated by an algorithmic method based on R-functions [53]. Actually, the max function used in the calculation of TDF value in conventional MMC-based TO [20,26,27,41] is a specific case of R-functions [54]. It is noted that R-functions are differentiable except for the cases of max and min function. Besides, during the shape optimization based on IGA proposed by Qian et al. [44], three collocation schemes based on uniform, Gauss and Greville abscissae leading to accurate and stable numerical analysis has been studied where the collocation scheme based on Greville abscissae leads to more accurate and robust analysis results than those based on uniform and Gauss. In the currently ITO-MMC, the ersatz material model is established on the control points, which is indirect and complicated. Inspired by the result mentioned above about the shape optimization based on IGA, three new ersatz material models based on uniform, Gauss and Greville abscissae collocation schemes will be proposed in this work.

To address the common problem aforementioned in both conventional MMC-based TO and ITO-MMC, a new method based on R-functions is presented to calculate the TDF values, by which the convergence rate of TO can be improved. Hence, based on R-functions and the ersatz material models, a general and new isogeometric explicit MMC optimization (ITO-MMC) method is proposed in this paper. In the reminder of this paper, Section 2 gives a brief introduction to the MMC-based TO, NURBS basis and R-function. Section 3 presents a general and new formulation of ITO-MMC using both R-functions and three new ersatz material models, and the specific form of ITO-MMC depends on the kind of new ersatz material model. Section 4 describes the unified analytical formulas for analysis and sensitivities of ITO-MMC over the three new ersatz material models. Section 5 discusses the results of benchmark examples TO problems implemented by the proposed method, and the conclusions are drawn in Section 6.

2. Theoretical basis

MMC-based TO, IGA and R-functions are the theoretical bases of this paper. For general discussion on MMC-based TO, IGA and R-functions, we refer readers to [20,21,27,55,31,37,39,53,54,56] and the references therein.

2.1. MMC-based TO

SIMP, evolutionary structural optimization and level set approach are major approaches for continuous structure TO. However, all the above methods lack explicit description of the geometric models, which makes the optimized results cannot be directly used for engineering applications without tedious postprocessing. To solve this problem, recently, Guo et al. [27] presented an explicit TO method based on MMC with straight skeleton and variable depth.

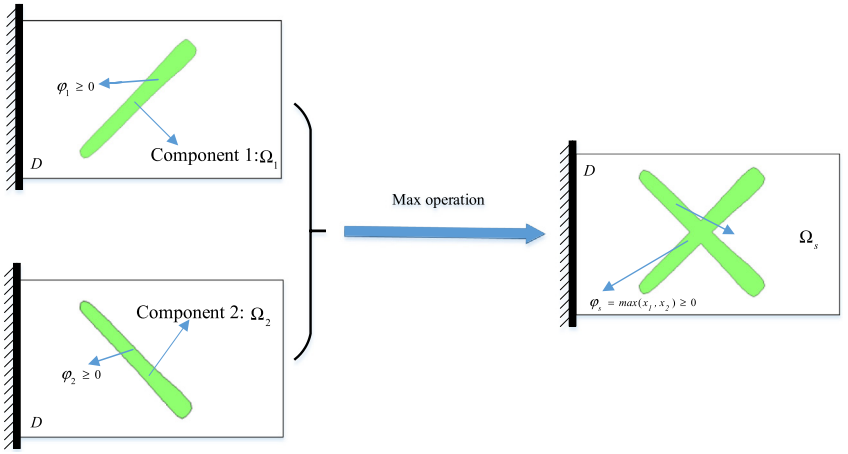

Fig. 2. The representation of structural topology through the max operation of TDF values of all components in the described domain.

2.1.1. *Geometric description of basic structural components*

As shown in Refs. [27,55,57], the geometric description of structural topology can be achieved by the follows:

$$\begin{cases} \varphi^s(x) > 0, & if\ x \in \Omega^s \\ \varphi^s(x) = 0, & if\ x \in \partial\Omega^s \\ \varphi^s(x) < 0, & if\ x \in D \setminus \Omega^s \end{cases} \tag{1}$$

where

$$\varphi^s(x) = \max(\varphi_1, \ldots, \varphi_n). \tag{2}$$

In Eq. (1), D represents a prescribed design domain and $\Omega^s \subset D$ denotes the solid material region which is a part of design domain and occupied by n basic solid structural components. The basic solid structural components may have the overlapping region during the optimization process. $\varphi^s(x) = \max(\varphi_1, \ldots, \varphi_n)$ with $\varphi_i = \varphi_i(x)$, $i = 1, 2, \ldots, n$ denoting the TDF of the region occupied by the ith component (i.e., Ω_i), is used to represent the TDF values of the overlapping region and non-overlapping region of structural components in a unified way and φ_i is formulated as:

$$\begin{cases} \varphi_i(x) > 0, & if\ x \in \Omega^s \\ \varphi_i(x) = 0, & if\ x \in \partial\Omega^s \\ \varphi_i(x) < 0, & if\ x \in D \setminus \Omega^s. \end{cases} \tag{3}$$

Obviously, $\Omega^s = \cup_{i=1}^{n} \Omega_i$ and the aforementioned max function of basic components can be viewed as a recursion of union operation of two components, that is $\Omega^s = \Omega^{s-1} \cup \Omega_n$ where $\Omega^{s-1} = \cup_{i=1}^{n-1} \Omega_i$. Fig. 2 shows a schematic illustration of the above geometry representation.

According the seminal work of Guo et al. [20,27], the TDF of component with straight skeleton and variable depth can be explicitly represented by the geometric information, which consists of the coordinates of center, half length, inclined angle, variable depth of the basic component. The TDF of the ith basic component is written as follows:

$$\varphi_i(x, y) = \left(\frac{x'}{L_i}\right)^p + \left(\frac{y'}{f(x')}\right)^p - 1 \tag{4}$$

with

$$\begin{Bmatrix} x' \\ y' \end{Bmatrix} = \begin{bmatrix} \cos\theta_i & \sin\theta_i \\ -\sin\theta_i & \cos\theta_i \end{bmatrix} \begin{Bmatrix} x - x_{0i} \\ y - y_{0i} \end{Bmatrix} \tag{5}$$

and

$$f(x') = \frac{t_{1i} + t_{2i} - 2t_{3i}}{2L_i^2}(x')^2 + \frac{t_{2i} - t_{1i}}{2L_i}x' + t_{3i}. \tag{6}$$

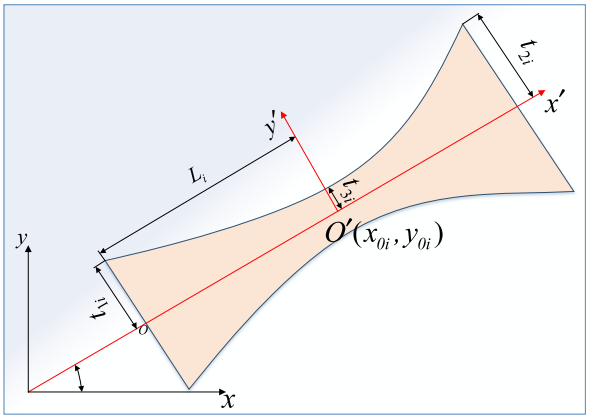

Fig. 3. Geometry description of the ith component with straight skeleton and quadratically variable depth.

In Eq. (4) p is a relatively larger even number ($p = 6$ in this paper) and the meaning of geometric parameters are illustrated in Fig. 3. Therefore, a structural component having similar shape as shown in Fig. 3 can be uniquely determined by a set of geometry parameters $\boldsymbol{D}_i = (x_{0i}, y_{0i}, L_i, t_{1i}, t_{2i}, t_{3i}, \theta_i)$. Furthermore, the structural topology can be explicitly and uniquely described by the vector of the design variables $\boldsymbol{D} = (\boldsymbol{D}_1^T, \boldsymbol{D}_2^T, \ldots, \boldsymbol{D}_n^T)^T$.

2.1.2. Problem formulation based on MMC

The general mathematical formulation of a MMC-based structural TO problem can be stated as follows

$$\begin{aligned} &Find\ \boldsymbol{D} = (\boldsymbol{D}_1^T, \boldsymbol{D}_2^T, \ldots, \boldsymbol{D}_n^T)^T \\ &Minimize\ I = I(\boldsymbol{D}) \\ &s.t. \\ &g_j(\boldsymbol{D}) \le 0 \quad j = 1, \ldots, m \\ &\boldsymbol{D} \subset \boldsymbol{U_D} \end{aligned} \tag{7}$$

where the objective function I is a function of the geometry variables $\boldsymbol{D}$ of all basic structural components, m is the number of inequality constraints, and $\boldsymbol{U_D}$ is the admissible set where $\boldsymbol{D}$ belongs.

To solve the generally nonlinear optimization problem, both gradient based and non-gradient methods can be utilized. In this work, we focus on a gradient based approach where both the structural response and its sensitivity over design variables are required. The specific optimization algorithm used in this paper is the method of moving asymptotes (MMA) [58].

A classical structural TO problem is minimizing the compliance of a structure under a fixed amount material through a volume fraction constraint $V \le V(\boldsymbol{D})$. Using the Galerkin numerical method, its discrete form is written as Eq. (8). In Eq. (8), f^i denote the body force density in Ω_i, t is the surface traction on Neumann boundary Γ_t. Moreover, it has been assumed that $\mathbb{E}(x) = \mathbb{E}^i$,

$$\begin{aligned} &Find\ \boldsymbol{D} = (\boldsymbol{D}_1^T, \boldsymbol{D}_2^T, \ldots, \boldsymbol{D}_n^T)^T, u(\boldsymbol{x}) \\ &Minimize\ C = \sum_{i=1}^{n} \int_{\Omega_i \setminus \bigcup_{1\le j<i} (\Omega_i \cap \Omega_j)} f^i \cdot u dV + \int_{\Gamma_t} t \cdot u dS \\ &s.t. \\ &\sum_{i=1}^{n} \int_{\Omega_i \setminus \bigcup_{1\le j<i} (\Omega_i \cap \Omega_j)} \mathbb{E}^i : \varepsilon(u) : \varepsilon(v) dV = \sum_{i=1}^{n} \int_{\Omega_i \setminus \bigcup_{1\le j<i} (\Omega_i \cap \Omega_j)} v \cdot f^i dV + \int_{\Gamma_t} t \cdot v dS\ , \forall v \in \boldsymbol{U}_{ad} \\ &V(\boldsymbol{D}) \le \overline{V}\ , \\ &\boldsymbol{D} \subset \boldsymbol{U_D}\ , \\ &u = \overline{u},\ on\ \Gamma_u \end{aligned} \tag{8}$$

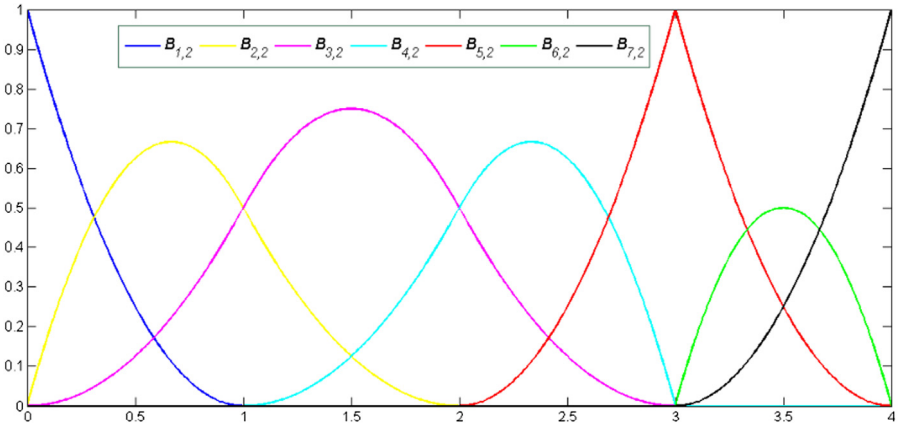

Fig. 4. All quadratic basis functions are constructed by the knot $\Xi = [0, 0, 0, 1, 2, 3, 3, 4, 4, 4]$. Each basic function $B_{i,2}$ (represented by different colors) can be generated by Eq. (10). (For interpretation of the references to color in this figure legend, the reader is referred to the web version of this article.)

$f = f^i$ if $x \in \Omega_i \setminus \bigcup_{1\le j<i}(\Omega_i \cap \Omega_j)$, with $i = 1, 2, \ldots, n$, and $\overline{u}$ is the prescribed displacement on Dirichlet boundary Γ_u. In addition, u and v are the displacement field and the corresponding test function defined on $\Omega^s = \cup_{i=1}^n \Omega_i$ with $\boldsymbol{U}_{ad} = \left\{v | v \in H^1(\Omega),\ v = 0 \text{ on } \Gamma_u\right\}$. The ε represents the second order linear strain tensor. $\mathbb{E}^i = E^i/(1+\nu^i)[\mathbb{I} + \nu^i/(1-2\nu^i)\delta \otimes \delta]$ ($\mathbb{I}$ and $\boldsymbol{\delta}$ are the fourth and the second order identity tensor, respectively) is the fourth order isotropic elasticity tensor of the material constituting the ith component. In the expression of $\mathbb{E}^i$, the symbols E^i and ν^i denote the corresponding Young's modulus and Poisson's ratio. The symbol $\overline{V}$ is the upper bound of the available volume of solid material. In the present work, it is assumed that $E^i = E$ and $\nu^i = \nu$, $i = 1, 2, \ldots, n$. For the sake of simplicity, we set $\overline{u} = 0$ in the following discussion.

It is noted that the C^1 discontinuity caused by the max function is neglected in conventional MMC-based TO, which apparently deteriorates the convergence of MMA-based TO.

2.2. Basic fundamentals of IGA

A commonly used method of generating and representing curves and surfaces is known as Non-uniform rational B-splines (NURBS), constructed from B-splines, in compute$R$-aided design (CAD) and computer graphics (CG) [59]. The (ordered) knot vector is introduced providing two positive integers p and n.

$$\boldsymbol{\Xi} := [\xi_1, \xi_2, \ldots, \xi_{n+p+1}] \text{ with } \xi_i \le \xi_{i+1} \forall i, \tag{9}$$

where p is the degree of the B-spline and n is the number of basis functions (also the number of control points), and the maximum multiplicity in a knot vector is $p + 1$. We only consider the case of open knot vectors in following contents for simplicity, in which the first and last knots have multiplicity $p + 1$. Given a knot vector $\boldsymbol{\Xi}$, univariate B-spline basis functions $B_{i,p}(\xi)$, $i = 1, 2, \ldots, n$, are defined recursively by the well known Cox–de Boor recursion formula [60]:

$$\begin{aligned} B_{i,0}(\xi) &= \begin{cases} 1 & if\ \xi_i \le \xi < \xi_{i+1} \\ 0 & \text{otherwise} \end{cases} \\ B_{i,p}(\xi) &= \frac{\xi - \xi_i}{\xi_{i+p} - \xi_i} B_{i,p-1}(\xi) + \frac{\xi_{i+p+1} - \xi}{\xi_{i+p+1} - \xi_{i+1}} B_{i+1,p-1}(\xi) \quad if \quad \xi_i \le \xi < \xi_{i+1} \end{aligned} \tag{10}$$

where we define the convention $0/0 = 0$. An example of spline basis functions are depicted in Fig. 4.

By introducing a positive weight w_i to each B-spline basis function, a NURBS basis function is defined as

$$N_{i,p}(\xi) = \frac{B_{i,p}(\xi) w_i}{\sum_{j=1}^n B_{j,p}(\xi) w_j}. \tag{11}$$

NURBS basis functions have many unique properties and four important among those are briefly listed here as: (1) Nonnegativity: $N_{i,p} \geq 0 \forall i$; (2) Partition of unity: $\sum_{i=1}^{n} N_{i,p} = 1$; (3) Local support: $N_{i,p}(\xi) = 0$ for $\xi \notin [\xi_i, \xi_{i+p+1})$; (4) Differentiability: $N_{i,p}(\xi)$ is $p - k$ times differentiable where k is the multiplicity of the knots.

To represent a surface, the tensor product formulation is adopted to construct two-dimensional basis NURBS basis functions of order p in ξ direction and q in η direction as

$$N_{i,p}^{j,q}(\xi, \eta) = N_{i,p}(\xi) N_{j,q}(\eta) \tag{12}$$

and a NURBS surface is a bivariate piecewise rational function of the form:

$$S(\xi, \eta) = \sum_{i=1}^{n} N_{i,p}^{j,q}(\xi, \eta) P_{i,j} \tag{13}$$

where $P_{i,j}$ are the control points, and the patch for this surface is $[\xi_1, \xi_2, \ldots, \xi_{n+p+1}] \times [\eta_1, \eta_2, \ldots, \eta_{m+q+1}]$. It is noted that the continuity and support of NURBS basis function are the same as for B-splines. Furthermore, B-splines can be seen as a special case of NURBS with all weights being equal to one.

2.3. Introduction to R functions

This subsection describes R-functions which can used as basic tool to compose a general function for the intersected surface of the objects [61] and presents some properties of R-functions as well.

The intersection or union of two primitive geometries having different explicit inequations can be expressed by a unified inequation which is obtained by corresponding boolean operation of primitive geometries. The boolean operation of different primitive geometries is not possible using polynomial functions, and the additional functions of geometry constructed by the boolean operation of different primitive geometries are required to have *p-roots* [54]. The requirement discussed early can be satisfied by R-functions formulated as:

$$\begin{aligned} R_{\cap}^{\alpha} &= \frac{1}{1+\alpha}\left(f_1 + f_2 - \sqrt{f_1^2 + f_2^2 - 2\alpha f_1 f_2}\right) \\ R_{\cup}^{\alpha} &= \frac{1}{1+\alpha}\left(f_1 + f_2 + \sqrt{f_1^2 + f_2^2 - 2\alpha f_1 f_2}\right) \end{aligned} \tag{14}$$

where f_1, f_2, $R_{\cap}^{\alpha}$, $R_{\cup}^{\alpha}$: $\mathbb{R}^n \rightarrow \mathbb{R}$, denote the explicit mathematical expression of the first, the second primitive, intersection and union geometry, respectively. Besides, parameter α ranges from -1 to 1. The expression of R-functions of two primitive geometries can be easily extended to multi geometry cases with a recursive form and it follows:

$$\begin{aligned} R^{\alpha}(\cap f_{i=1}^{n}) &= \frac{1}{1+\alpha}\left(R^{\alpha}(\cap f_{i=1}^{n-1}) + f_n - \sqrt{(R^{\alpha}(\cap f_{i=1}^{n-1}))^2 + f_n^2 - 2\alpha R^{\alpha}(\cap f_{i=1}^{n-1}) f_n}\right) \\ R^{\alpha}(\cup f_{i=1}^{n}) &= \frac{1}{1+\alpha}\left(R^{\alpha}(\cup f_{i=1}^{n-1}) + f_n + \sqrt{(R^{\alpha}(\cup f_{i=1}^{n-1}))^2 + f_n^2 - 2\alpha R^{\alpha}(\cup f_{i=1}^{n-1}) f_n}\right) \\ &\text{with} \\ R^{\alpha}(\cap f_{i=1}^{n-1}) &= \frac{1}{1+\alpha}\left(R^{\alpha}(\cap f_{i=1}^{n-2}) + f_{n-1} - \sqrt{(R^{\alpha}(\cap f_{i=1}^{n-2}))^2 + f_{n-1}^2 - 2\alpha R^{\alpha}(\cap f_{i=1}^{n-2}) f_{n-1}}\right) \\ R^{\alpha}(\cup f_{i=1}^{n-1}) &= \frac{1}{1+\alpha}\left(R^{\alpha}(\cup f_{i=1}^{n-2}) + f_{n-1} + \sqrt{(R^{\alpha}(\cup f_{i=1}^{n-2}))^2 + f_{n-1}^2 - 2\alpha R^{\alpha}(\cup f_{i=1}^{n-2}) f_{n-1}}\right). \end{aligned} \tag{15}$$

In Eq. (15), f_{n-1} is the $(n-1)$th geometry, f_n denotes the nth geometry, $R^{\alpha}(\cap f_{i=1}^{n-2})$ is the intersection of the first $(n-2)$ primitive geometries, the intersection of the first $(n-1)$ primitive geometries is $R^{\alpha}(\cap f_{i=1}^{n-1})$, $R^{\alpha}(\cap f_{i=1}^{n})$ represents the intersection of all primitive geometries, the union of the first $(n-2)$ primitive geometries is expressed by $R^{\alpha}(\cup f_{i=1}^{n-2})$, $R^{\alpha}(\cup f_{i=1}^{n-1}))$ is the union of the first $(n-1)$ primitive geometries, $R^{\alpha}(\cup f_{i=1}^{n})$ represents the union of the all primitive geometries. A 1×2 rectangle region can be described by the intersection region $R_{\cap}^{\alpha} = \bigcap_{i=1}^{4} f_i$ ($\alpha = 0$ or 1) of four different primitive geometries which have explicit mathematic expression of $f_1 = (1 - x) \geq 0$, $f_2 = (1 + x) \geq 0$, $f_3 = (1 - y) \geq 0$ and $f_4 = (1 - y) \geq 0$, respectively. The rectangle

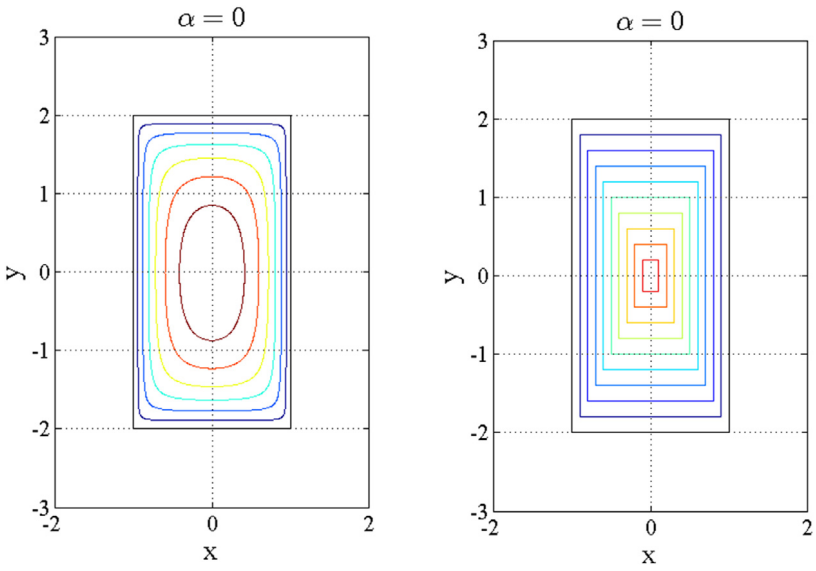

Fig. 5. An illustration of rectangle region described by the intersection of four regions, with $\alpha = 0$ in the left and $\alpha = 1$ in the right.

region is as depicted in Fig. 5. Then an illustration of union and intersection of two rectangle with size of 1×2 and 2×1 are presented in Fig. 6.

Two important remarks of R-functions are briefly listed here as:

Remark 1. max and min functions are a subset of R-functions. It is noted that in case of $\alpha = 1$, Eq. (14) for intersection, union can be simplified to $R^{\alpha}_{\cap} = \frac{1}{2}(f_1 + f_2 - |f_1 - f_2|) = \min(f_1, f_2)$ and $R^{\alpha}_{\cap} = \frac{1}{2}(f_1 + f_2 + |f_1 - f_2|) = \max(f_1, f_2)$, respectively.

Remark 2. R-functions are differentiable for $\alpha \in (-1, 1) \in \mathbb{R}$. In other words, R-functions are C^1 continuous except for max and min function.

3. A general and new formula of ITO-MMC

Based on R-functions and collocation points, a general and new ITO-MMC formula with three different forms is presented in this section, which is different from that proposed in [28]. In the new formula of ITO-MMC, the TDF are calculated by R-functions. After that, three new ersatz material models are proposed based on the uniform distribution, Gaussian quadrature and Greville abscissae in a unified expression. In the end, the three new ersatz material models are used in the general and new ITO-MMC formula.

3.1. Geometric description of components based on R-functions

The max function to compute the TDF values is not differentiable in conventional MMC-based TO and ITO-MMC proposed in [28]. In order to solve the C^1 discontinuity problem in the MMC-based TO and ITO-MMC theoretically, we replace the max function with R-functions. Recalling that the TDF of the ith basic component is remain unchanged. Namely, the way to compute the TDF values with respect to individual component is the same as Eqs. (4), (5), (6) in the new formula ITO-MMC, but the union TDF value from the TDF values of all components is computed as:

$$\begin{aligned}
&\varphi^s = \begin{cases} R^{\alpha}(\cup\varphi_{i=1}^{m}) & if\ \varphi_i \in \varphi_+\ with\ 2 \le m \le n \\ \max(\varphi_1, \varphi_2, \ldots, \varphi_n) & otherwise \end{cases} \\
&with\ \varphi_+ = \{\varphi_i \in \{\varphi_1, \varphi_2, \ldots, \varphi_n\} | \varphi_i > 0\} \\
&R^{\alpha}(\cup\varphi_{i=1}^{m}) = \frac{1}{1+\alpha}\left(R^{\alpha}(\cup\varphi_{i=1}^{m-1}) + \varphi_m + \sqrt{(R^{\alpha}(\cup\varphi_{i=1}^{m-1}))^2 + \varphi_m^2 - 2\alpha R^{\alpha}(\cup\varphi_{i=1}^{m-1})\varphi_m}\right)\ \alpha \in (-1, 1)
\end{aligned} \tag{16}$$

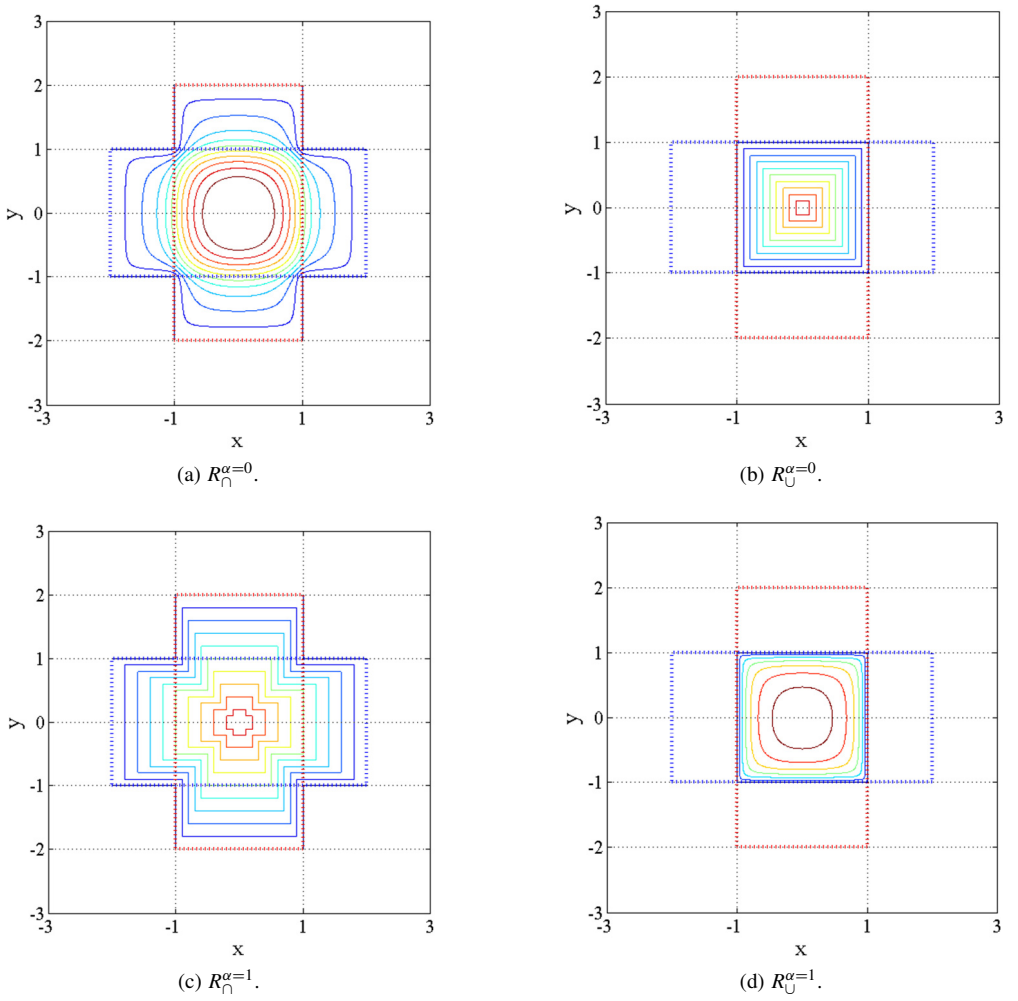

(a) $R_{\cap}^{\alpha=0}$. (b) $R_{\cup}^{\alpha=0}$.

(c) $R_{\cap}^{\alpha=1}$. (d) $R_{\cup}^{\alpha=1}$.

Fig. 6. Four contour maps of geometries which are constructed by R-functions for different cases are presented here: (a) is the intersection of two rectangles with $\alpha = 0$, (b) is the union of two rectangles with $\alpha = 0$, (c) is the intersection of two rectangles with $\alpha = 1$, (d) is the union of two rectangles with $\alpha = 1$.

where φ_+ represents a subset of $\{\varphi_1, \varphi_2, \ldots, \varphi_n\}$ and the values of elements in φ_+ (the element number is m) are greater than zero. The TDF values are calculated by R-functions in the overlapping region of components. The max function is still used in the region in which the components are not intersected or the TDF values with respect to all the components are less or equal than zero. According to Remark 2 in Section 2.3, the C^1 continuity in the structure during the TO process is achieved by the use of R-functions. We illustrate the union geometry of two intersected components in Fig. 7 and the mathematical expression of the union geometry is calculated from those of two intersected components with the use of R-functions ($\alpha = 0$).

3.2. Three new ersatz material models based on collocation points

In the ITO-MMC proposed in [28], the ersatz material model is derived by the Heaviside values of the control points and the NURBS basis functions. It is depicted in Fig. 8.

In contrast to the indirect way of representing the ersatz material model from the control points and inspired by the numerical results of the IGA collocation schemes in [44], three new ersatz material models are devised, which are

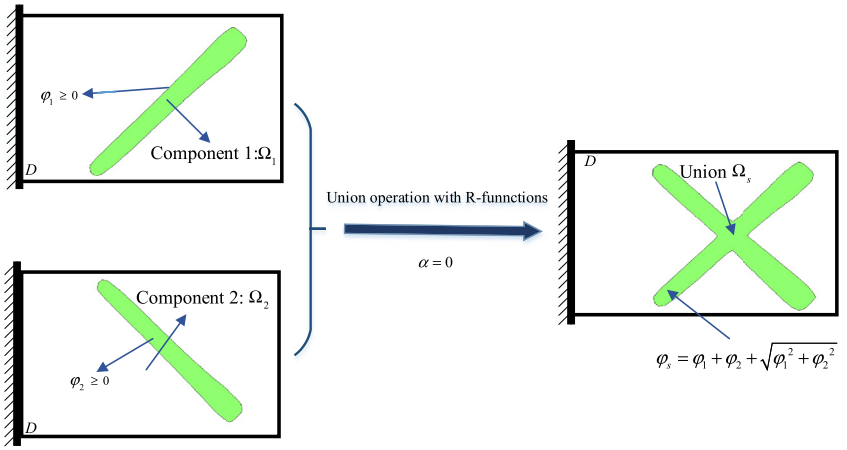

Fig. 7. An illustration of the union geometry of two intersected components using R-functions.

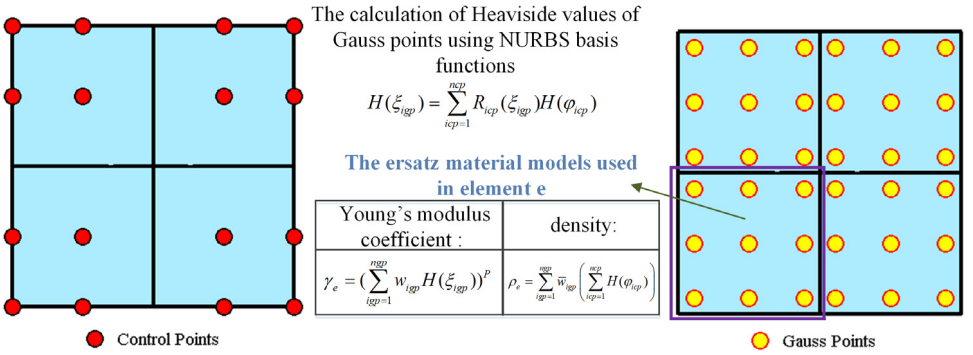

Fig. 8. The ersatz material model used in [28] for NURBS elements in the rectangle design domain.

based on uniform, Gauss and Greville abscissae collocation schemes, respectively. The collocation schemes mentioned above are shown as follows:

- **a.** Uniform distribution where the collocation points correspond to a sequence of points located on equally spaced position in the parameter domain.
- **b.** Gaussian quadrature where the collocation points are a number of Gaussian points obtained by transforming the Gaussian quadrature points from $[-1, 1]$ to the patch parameter domain.
- **c.** Greville abscissae where the parameters correspond to collocation points for a *degree-p* NURBS with n control points and a length of $n + p + 1$ knot vector $\Xi = [\xi_1, \xi_2, \ldots, \xi_{n+p+1}]$ are defined as [62,63]:

$$\zeta_i = \frac{1}{p}(\xi_{i+1} + \xi_{i+2} + \cdots \xi_{i+p}) i = 1, 2, \ldots, n. \tag{17}$$

The key point in traditional MMC-based TO is the ersatz material model defined by the nodal points of the element. According to the result of the shape optimization based on IGA proposed by Qian et al. [44], where three collocation schemes based on uniform, Gauss and Greville abscissae are used to carry on the isogeometric computations, it shows that Greville abscissae leads to more accurate and robust analysis results than those based on uniform and Gauss. Analogously, the points used to define the ersatz material model of MMC-based TO may has an impact on the convergence process of MMC-based TO due to the different numerical performance of different collocation points. Therefore, to reveal the effects of the different types points on the convergence rate of the MMC-based TO, three new ersatz material models mentioned above are proposed and compared in the benchmark.

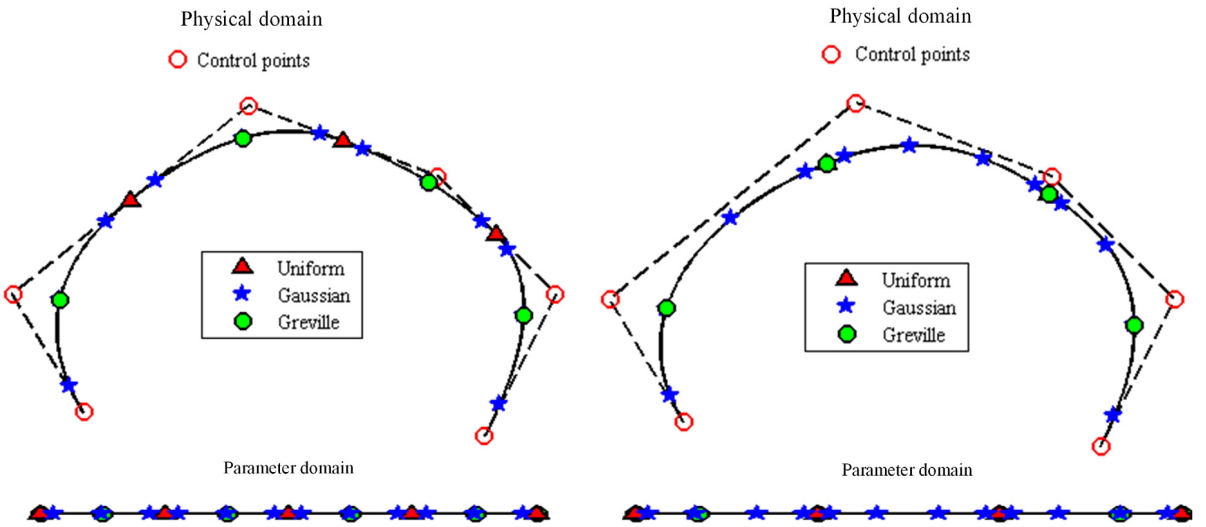

(a) $p = 2, n_{cp} = 6, \xi_1 = [0\,0\,0\,1/4\,1/2\,3/4\,1\,1\,1]$. (b) $p = 3, n_{cp} = 6, \xi_2 = [0\,0\,0\,0\,1/3\,2/3\,1\,1\,1\,1]$.

Fig. 9. Three collocation schemes: uniform distribution, Gaussian quadrature and Greville abscissae for quadratic and cubic NURBS with $n_{cp} = 6$ control points defined on knot vector $\Xi_1 = [0\,0\,0\,1/4\,1/2\,3/4\,1\,1\,1]$ and $\Xi_2 = [0\,0\,0\,0\,1/3\,2/3\,1\,1\,1\,1]$, respectively. (The first and last collocation points are the two clamped control points for uniform distribution, Greville abscissae schemes and are not shown.)

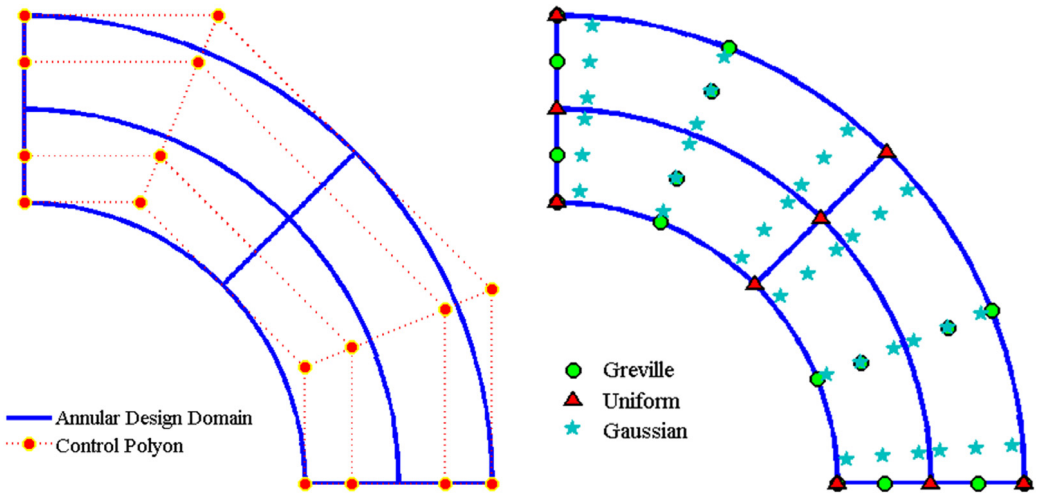

Fig. 10. An annular design domain is presented in the left and collocation points generated by three schemes are shown in the right for two identical knot vectors $\Xi_1 = \Xi_2 = [0\,0\,0\,1/2\,1\,1\,1]$.

In general, the collocation points are different under these three collocation schemes. In both physical and parameter domain, the collocation points generated by the three schemes are shown in Fig. 9 for both quadratic and cubic NURBS curves. Furthermore, the position of three different types collocation points for a annular design domain discretized by four elements are illustrated in Fig. 10.

After getting the three different types of collocation points, the three new ersatz material models are obtained as follows. Firstly, we calculate the TDF values of collocation points by Eq. (16). Secondly, the Heaviside values of collocation points are obtained by the regularized Heaviside function formulated as Eq. (18). Thirdly, the three different Young's modulus coefficients and densities of the corresponding ersatz material models are calculated from the Heaviside values of corresponding collocation points. Lastly, the three new ersatz material model are be expressed

in a unified formula and are formulated as Eq. (19).

$$H_\varepsilon(x) = \begin{cases} 1 & if\ x > \varepsilon \\ \dfrac{3(1-\beta)}{4}\left(\dfrac{x}{\varepsilon} - \dfrac{x^3}{3\varepsilon^3}\right) + \dfrac{1+\beta}{2} & if\ -\varepsilon \le x \le \varepsilon \\ \beta & if\ x < -\varepsilon. \end{cases} \tag{18}$$

In Eq. (18), β is a small positive parameter, which ensure the nonsingularity of global stiffness matrix, and the level of regularization is controlled by ε.

$$\begin{cases} \gamma^i = \dfrac{1}{n^i_{col}}\left(\displaystyle\sum_{icol=1}^{n^i_{col}} H^q_\varepsilon(\varphi^i_{icol})\right) \\ \rho^i = \dfrac{1}{n^i_{col}}\left(\displaystyle\sum_{icol=1}^{n^i_{col}} H_\varepsilon(\varphi^i_{icol})\right) \end{cases} i = 1, 2, 3. \tag{19}$$

In Eq. (19), γ^i and ρ^i represent the ith type Young's modulus coefficient and density of NURBS element, n^i_{col} means the number of ith type collocation points corresponding to the element, φ^i_{icol} is the TDF value of $icol$th collocation point, $q = 2$, $H_\varepsilon(\varphi_{icol})$ is the regularized Heaviside value of $icol$th collocation point, $i = 1, 2, 3$ correspond to uniform, Gauss and Greville abscissae collocation scheme, respectively.

3.3. A general and new formula of ITO-MMC

The three new ersatz material models based on collocation points are shown in Section 3.2 such that the formula presented in Eq. (8) for the minimum compliance problem with a prescribed volume constraint in the ITO-MMC can be reformulated as follows:

$$\begin{aligned} &Find\ \boldsymbol{D} = (\boldsymbol{D}_1^T, \boldsymbol{D}_2^T, \ldots, \boldsymbol{D}_n^T)^T,\ \boldsymbol{u}(\boldsymbol{x}) \\ &Minimize\ C = \sum_{e=1}^{N_e} \gamma_e^i \boldsymbol{u}_e^T \boldsymbol{K}_e \boldsymbol{u}_e \\ &s.t. \\ &(\sum_{e=1}^{N_e} \gamma_e^i \boldsymbol{K}_e) \cdot \boldsymbol{u} = \boldsymbol{F} \\ &\sum_{e=1}^{N_e} \rho_e^i V_e \le \overline{V} \\ &\boldsymbol{D} \subset \boldsymbol{U_D} \\ &i = 1, 2, 3 \end{aligned} \tag{20}$$

where $\boldsymbol{D}$ is a set consisting of the geometric design variables of all components, $\boldsymbol{u}(\boldsymbol{x})$ is the displacement field of the design domain, C is the mean compliance of the structure, γ_e^i and ρ_e^i are the Young's modulus coefficient and density of the eth NURBS element, respectively, $\boldsymbol{u}_e$ is the displacement vector corresponding to the eth NURBS element, $\boldsymbol{K}_e$ is the stiffness matrix of eth NURBS element where the Young's modulus is equal to 1, $\boldsymbol{F}$ is the external load vector, V_e is the eth element volume, $\overline{V}$ is the prescribed volume fraction, $\boldsymbol{U_D}$ is the admissible set to which $\boldsymbol{D}$ belongs, $i = 1$ is the ersatz material model based on uniform collocation scheme, $i = 2$ denotes that based on Gauss collocation scheme and $i = 3$ represents that based on Greville abscissae collocation scheme in this paper.

4. Numerical implementation

4.1. Isogeometric analysis

The minimum compliance problem under a volume constraint is solved by the ITO method. The discrete equilibrium equation may be reformulated as [28]

$$\boldsymbol{K}\boldsymbol{u} = \boldsymbol{F}, \tag{21}$$

in which $\boldsymbol{K}$ is stiffness matrix, $\boldsymbol{u}$ is the displacement vector and $\boldsymbol{F}$ is the external force vector associated with the control points. The stiffness matrix is made of the element stiffness matrix $\boldsymbol{K}_e$ which is formulated as

$$\begin{aligned}\boldsymbol{K}_e &= \int_{\Omega_e} \boldsymbol{B}^T\boldsymbol{D}\boldsymbol{B}d\Omega \\ &= \int_{\hat{\Omega}_e} \boldsymbol{B}^T\boldsymbol{D}\boldsymbol{B}|J_1|d\hat{\Omega} \\ &= \int_{\overline{\Omega}_e} \boldsymbol{B}^T\boldsymbol{D}\boldsymbol{B}|J_1||J_2|d\overline{\Omega}\end{aligned} \tag{22}$$

where $\boldsymbol{B}$ is strain–displacement matrix, $\boldsymbol{D}$ is stress–strain matrix, Ω_e is the domain of element, $\hat{\Omega}_e$ is the parametric domain in the NURBS parametric space $\{\xi, \eta\}$ and $\overline{\Omega}$ is the integration parametric space $\{\overline{\xi}, \overline{\eta}\}$. The transformation relation from the NURBS parametric space to the physical space and the integration parametric space to the NURBS parametric space are corresponding to J_1 and J_2, respectively.

For sake of simplicity, we only consider 2D plane stress problems in this part. Thus, the strain–displacement matrix $\boldsymbol{B}$ is written as

$$\boldsymbol{B} = \begin{bmatrix} \dfrac{\partial N_1}{\partial x} & 0 & \cdots & \dfrac{\partial N_{ne}}{\partial x} & 0 \\ 0 & \dfrac{\partial N_1}{\partial y} & \cdots & 0 & \dfrac{\partial N_{ne}}{\partial x} \\ \dfrac{\partial N_1}{\partial x} & \dfrac{\partial N_1}{\partial y} & \cdots & \dfrac{\partial N_{ne}}{\partial x} & \dfrac{\partial N_{ne}}{\partial y} \end{bmatrix} \tag{23}$$

and

$$\begin{bmatrix} \dfrac{\partial N_i}{\partial x} \dfrac{\partial N_i}{\partial y} \end{bmatrix} = \begin{bmatrix} \dfrac{\partial N_i}{\partial \xi} \dfrac{\partial N_i}{\partial \eta} \end{bmatrix} J_1^{-1} \tag{24}$$

where N_i is a basis function in the NURBS patch and the Jacobian J_1 is formulated as

$$J_1 = \begin{bmatrix} \dfrac{\partial x}{\partial \xi} \dfrac{\partial y}{\partial \eta} \end{bmatrix}. \tag{25}$$

And, the stress–strain matrix $\boldsymbol{D}$ is

$$\boldsymbol{D} = \frac{E}{1-v^2} \begin{bmatrix} 1 & v & 0 \\ v & 1 & 0 \\ 0 & 0 & \dfrac{1-v}{2} \end{bmatrix} \tag{26}$$

where E is the elastic modulus and v is Poisson's ratio.

The mapping from the Gauss quadrature domain $[-1, 1]$ to the NURBS parametric domain $[\xi_i, \xi_{i+1}) \times [\eta_j, \eta_{j+1})$ is given by

$$\begin{cases} \xi = \dfrac{\xi_{i+1} - \xi_i}{2}(\overline{\xi} - 1) + \xi_i \\ \eta = \dfrac{\eta_{j+1} - \eta_j}{2}(\overline{\eta} - 1) + \eta_j. \end{cases} \tag{27}$$

Thus, the Jacobian J_2 may be written as:

$$J_2 = \begin{bmatrix} \frac{\partial \xi}{\partial \overline{\xi}} & \frac{\partial \eta}{\partial \overline{\xi}} \\ \frac{\partial \xi}{\partial \overline{\eta}} & \frac{\partial \eta}{\partial \overline{\eta}} \end{bmatrix} = \begin{bmatrix} \frac{\xi_{i+1} - \xi_i}{2} & 0 \\ 0 & \frac{\eta_{i+1} - \eta_i}{2} \end{bmatrix}. \tag{28}$$

With use of the ersatz material model, as shown in (19), once the values of TDF at corresponding collocation points of a element are known, the Young's modulus of element can be interpreted as

$$E_e^i = E\gamma_e^i \tag{29}$$

where γ_e^i is the Young's modulus coefficient defined in Eq. (19). Then, the element stiffness $\overline{\boldsymbol{K}}_e^i$ used in the numerical implementation is formulated as:

$$\overline{\boldsymbol{K}}_e^i = \int_{\overline{\Omega}_e} \boldsymbol{B}^T \boldsymbol{D} \boldsymbol{B} |J_1||J_2| \frac{E_e^i}{E} d\overline{\Omega} = \int_{\overline{\Omega}_e} \boldsymbol{B}^T \boldsymbol{D} \boldsymbol{B} |J_1||J_2| \gamma_e^i d\overline{\Omega} = \boldsymbol{K}_e \gamma_e^i, \tag{30}$$

where $\boldsymbol{K}_e$ is the stiffness matrix of a fully solid element defined in Eq. (22). Obviously, the general and new formula of ITO-MMC based on R-functions and collocation points presented in Eq. (20) can be reformulated as:

$$\begin{aligned} &Find\, \boldsymbol{D} = (\boldsymbol{D}_1^T, \boldsymbol{D}_2^T, \ldots, \boldsymbol{D}_n^T)^T \,, \boldsymbol{u}(\boldsymbol{x}) \\ &Minimize\, C^i = \sum_{e=1}^{N_e} \boldsymbol{u}_e^T \overline{\boldsymbol{K}}_e^i \boldsymbol{u}_e \\ &s.t. \\ &\sum_{e=1}^{N_e} \overline{\boldsymbol{K}}_e^i \boldsymbol{u}_e = \boldsymbol{F} \\ &\sum_{e=1}^{N_e} \rho_e^i V_e \le \overline{V}\,, \\ &\boldsymbol{D} \subset \boldsymbol{U}_{\boldsymbol{D}} \\ &i = 1, 2, 3 \end{aligned} \quad , \tag{31}$$

where C^i is the mean compliance of the structure corresponding to the ith type collocation scheme.

4.2. Sensitivity design

For minimal compliance problem with available material constraint, the derivate of compliance C about a geometric design variable of a component can be obtained by differentiating both sides of

$$C^i = \sum_{e=1}^{N_e} \boldsymbol{u}_e^T \overline{\boldsymbol{K}}_e^i \boldsymbol{u}_e \;\; i = 1, 2, 3 \tag{32}$$

with respect to a_j denoted an arbitrary design variable, and it is written as

$$\frac{\partial C^i}{\partial a_j} = \sum_{e=1}^{N_e} \frac{\partial (\boldsymbol{u}_e^T \overline{\boldsymbol{K}}_e^i \boldsymbol{u}_e)}{\partial a_j} = \sum_{e=1}^{N_e} \left(\frac{\partial \boldsymbol{u}_e^T}{\partial a_j} \overline{\boldsymbol{K}}_e^i \boldsymbol{u}_e + \boldsymbol{u}_e^T \frac{\partial \overline{\boldsymbol{K}}_e^i}{\partial a_j} \boldsymbol{u}_e + \boldsymbol{u}_e^T \overline{\boldsymbol{K}}_e^i \frac{\partial \boldsymbol{u}_e}{\partial a_j} \right) \quad i = 1, 2, 3. \tag{33}$$

According the adjoint sensitivity analysis, the formulation above can be rewritten as

$$\frac{\partial C^i}{\partial a_j} = -\sum_{e=1}^{N_e} \left\{ \boldsymbol{u}_e^T q \cdot \frac{1}{n_{col}^i} \left(\sum_{icol=1}^{n_{col}^i} H_\varepsilon(\varphi_{icol}^i)^{q-1} \frac{\partial H_\varepsilon(\varphi_{icol}^i)}{\partial a_j} \right)_e \cdot \boldsymbol{K}_e \boldsymbol{u}_e \right\} \quad i = 1, 2, 3. \tag{34}$$

The $\frac{\partial H_\varepsilon(\varphi_{icol}^i)}{\partial a_j}$ in Eq. (34) is calculated by the finite difference quotient of φ_{icol}^i approximately here.

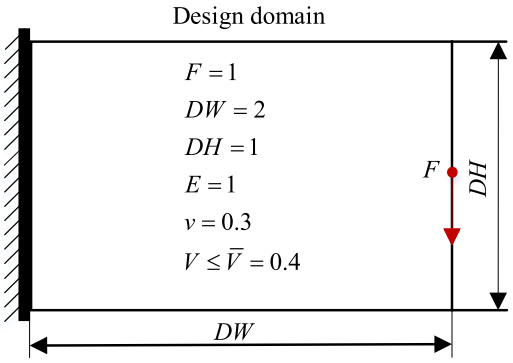

Fig. 11. The cantilever beam problem in 2D.

In addition, the sensitivity of the volume constraint function is formulated as

$$\frac{\partial V^i}{\partial a_j} = \sum_{e=1}^{N_e} \left(\frac{1}{n^i_{col}} \left(\sum_{icol=1}^{n^i_{col}} \frac{\partial H(\varphi^i_{icol})}{\partial a_j} \right) V_e \right)_e \quad i = 1, 2, 3. \tag{35}$$

5. Numerical examples

In order to verify the effectiveness of R-functions and make a comparison over the three new ersatz material models used in the new ITO-MMC as well as demonstrating the high efficiency of IGA, three benchmark problems are tested in this Section. The material properties, geometry data and external load are dimensionless parameters since only numerical performances are concerned. In the following tests, the Young's modulus and Poisson's ratio used in standard elasticity matrix Eq. (26) are chosen as $E = 1$ and $v = 0.3$. To solve the optimization problem numerically, the Method of Moving Asymptotes(MMA) [58] is used as the optimizer. All the examples are run on a laptop: the CPU is an Intel core i7 7500U 2.7 GHz, the RAM is 8 GB, the OS is Windows 10, and the software environment is MATLAB 2014a.

5.1. The cantilever beam problem

The cantilever beam are two of the most widely used TO benchmarks [64–66], which is used to verify the effectiveness of R-function under the FEM framework. And, two and three dimensional cases are taken into consideration in this paper. Moreover, the parameters of MMA used in this subsection are epsimin $= 10^{-10}$, raa0 $= 0.01$, albefa $= 0.4$, asyinit $= 0.1$, asyincr $= 0.8$, asydecr $= 0.6$.

5.1.1. Two dimensional case

The problem setting of the two dimensional cantilever beam benchmark is illustrated in Fig. 11. And, the dimension of the cantilever beam is assumed to be 2×1. The left end of the cantilever beam is clamped, and the center of the right-end edge is prescribed with external load F. The remaining edge is assumed as a free surface with zero applied tractions. The volume fraction of the solid material to be preserved is set to 40%. In order to ensure the effectiveness of R-functions under different mesh size, we compare the convergence rate between max function and R-functions in the cases where the design domain is discretized by bilinear FE elements with mesh size 60×30, 80×40 and 100×50, respectively.

First of all, the basic components used in the MMC-based TO should have an initial design. The initial design of rectangular components is same as that in [27], and it depicts two initial designs for the cantilever beam in Fig. 12. The two initial designs based on max function and R-functions shown in Fig. 12 are very similar. The final optimal structural topologies of max function and R-functions under different mesh sizes are shown in Fig. 13 and the values of objective functional are presented in the bottom of corresponding structures. From final optimal structural topologies

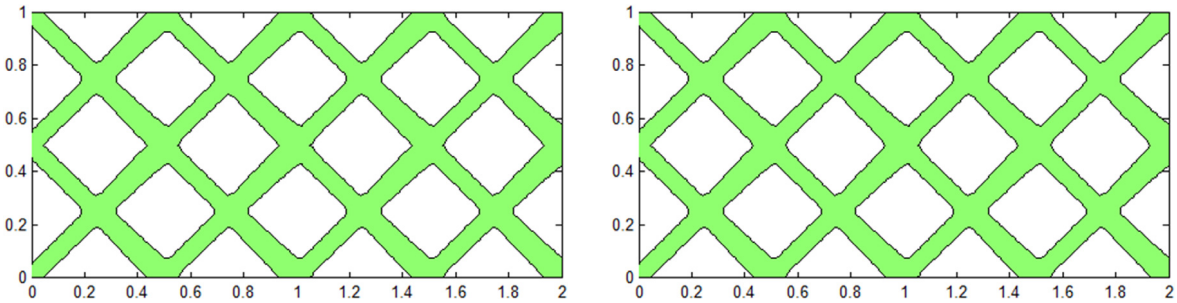

(a) Initial design for short beam example using max function. (b) Initial design for short beam example using R-functions.

Fig. 12. The initial design of basic components for max function and R-functions are shown in (a) and (b), respectively.

Table 1
The total iteration steps of optimization process based on max function and R-functions.

Mesh size	60×30	80×40	100×50
Total iteration steps using max function	464	244	841
Total iteration steps using R-functions	291	184	542
The improvement of the convergence rate $(\frac{step_{max}-step_{R\text{-}functions}}{step_{max}} \times 100\%)$	37.3%	24.6%	35.6%

and the values of objective functional, we can find that using R-functions is a feasible approach to replace the max function in computing the values of TDF for the overlapping region of basic structural components. According to the comparisons of total iteration steps (used to evaluate the convergence rate) between max function and R-functions summarized in Table 1, it is clearly shown that the convergence using R-functions is faster than that using max function. Compared to max function, calculating the TDF values with Eq. (15) based on R-functions can reduce the total iteration steps by 173, 60, 299 and increase the convergence rate by 37.3%, 24.6%, 35.6% for FE mesh with size of 60×30, 80×40, 100×50, respectively. It demonstrates that the C^1 introduced by R-functions in the structure can improve the convergence rate of MMC-based TO and the improvement is about 25%–40% for different mesh sizes. Thus, in the conventional MMC-based TO, using Eq. (15) based on R-functions is better than max function for calculating the TDF values.

Other issues shown in Table 1 are as follows. First of all, different mesh size has different convergence rate. Then, the design domain discretized by a FE mesh with size of 80×40 have the least total iteration steps in both max function and R-functions cases. Finally, according to the issues mentioned above, it could be concluded that the mesh size (i.e., the DOFs) has a big influence on the convergence rate.

5.1.2. Three dimensional case

The three dimensional cantilever problem setting is depicted in Fig. 14. Uniform linear distributed loads are placed in the middle line of the right face and the left face are fixed. To discretize the design domain, $80 \times 40 \times 8$ linear hexahedral elements are used. The volume fraction of the solid material to be preserved is set to 40%.

For sake of simplicity, the three dimensional rectangular components used in this paper are similar to those used in [55], of which the depth are invariant and equal to the depth (DT) of the design domain. The initial designs of structural components for max function together with that for R-functions are illustrated in Fig. 15.

The final structural topologies of three dimensional cantilever can be obtained by resorting to the MMC-based TO framework, and are presented in Fig. 16. It is obvious that the final optimized structure by R-functions are very similar to that obtained by max function. Moreover, the ratio of objective function by R-functions to that by max function is $ratio = \frac{Compliance_{R\text{-}functions}}{Compliance_{\max}} = 1.003$, which indicates that from the viewpoint of objective function, there is no difference in R-functions and max function under the framework of MMC-based TO. However, the number of iterations of R-functions is only 101, which are much less than 247 (the number of iterations of MMC-based TO using max function). In other words, MMC-based TO using R-functions can speed up the convergent rate of the traditional

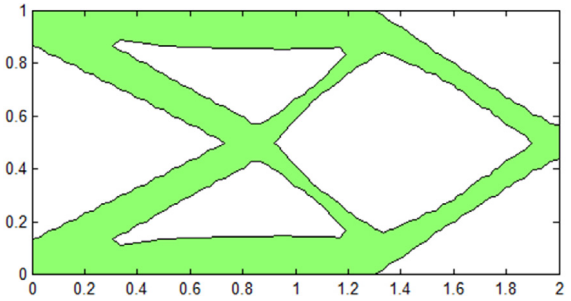

(a) Optimal structure of 60 × 30 FE mesh using max function the value of objective functional $C = 76.52$.

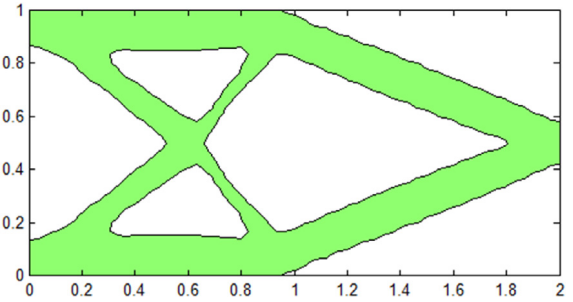

(b) Optimal structure of 60 × 30 FE mesh using R-functions the value of objective functional $C = 76.65$.

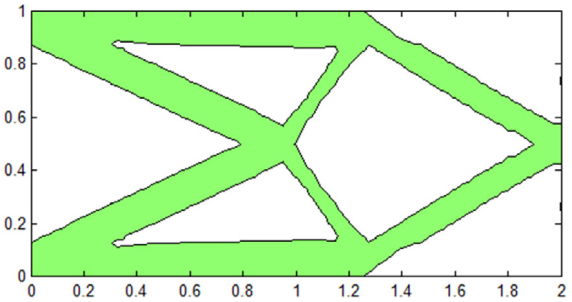

(c) Optimal structure of 80 × 40 FE mesh using max function the value of objective functional $C = 74.68$.

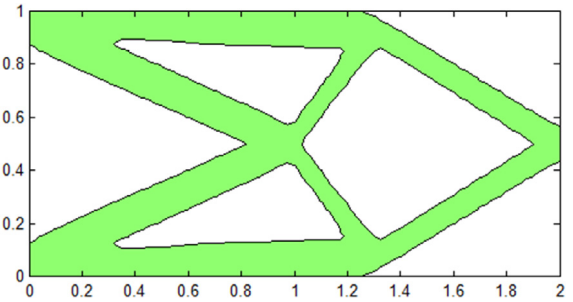

(d) Optimal structure of 80 × 40 FE mesh using R-functions the value of objective functional $C = 74.43$.

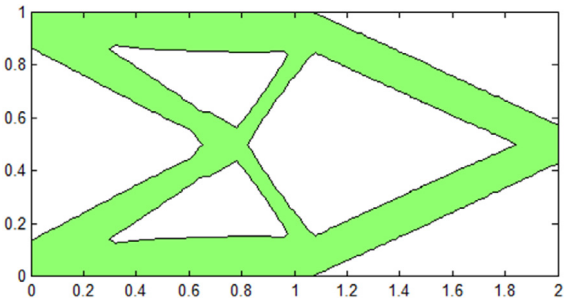

(e) Optimal structure of 100 × 50 FE mesh using max function the value of objective functional $C = 74.66$.

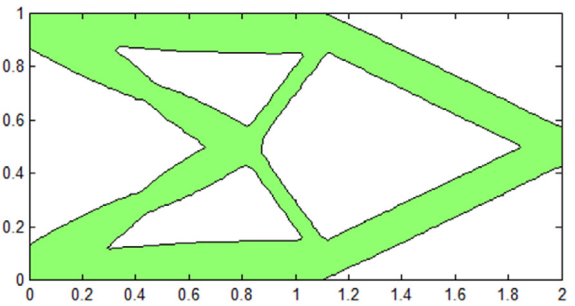

(f) Optimal structure of 100 × 50 FE mesh using R-functions the value of objective functional $C = 74.49$.

Fig. 13. The TO results of the max function and R-functions with different FE meshes: (a) max function with a FE mesh 60 × 30, (b) R-functions with a FE mesh 60 × 30, (c) max function with a FE mesh 80 × 40, (d) R-functions with a FE mesh 80 × 40, (e) max function with a FE mesh 100 × 50, (f) R-functions with a FE mesh 100 × 50.

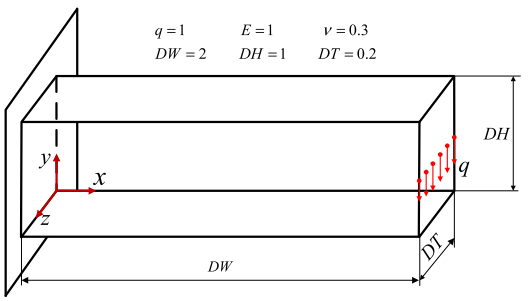

Fig. 14. Three dimensional cantilever problem setting.

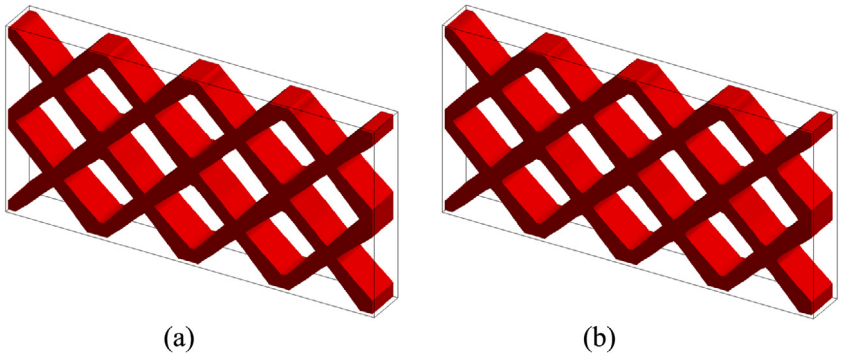

Fig. 15. The initial designs of three dimensional components: (a) for max function and (b) for R-functions.

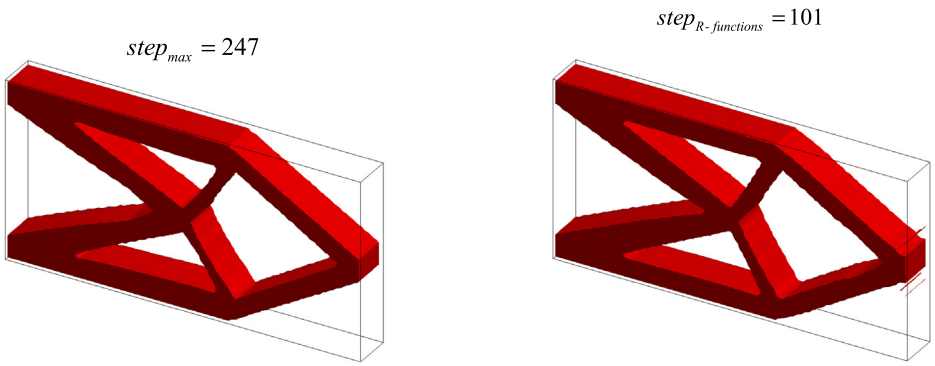

(a) $Compliance_{max} = 750.66$. (b) $Compliance_{R\text{-}functions} = 752.61$.

Fig. 16. Two illustrative results are depicted, and (a) is the final optimized structure by MMC-based TO using max function, as well as the topology optimized by MMC-based TO using R-functions is shown in (b).

MMC-based TO by 59.1% (calculated by Eq. (36)) without deteriorating the final optimized structural performance. Hence, the same conclusion that R-functions is an optimal choice compared to max function can be drawn here.

$$rate_{improvement} = \frac{step_{\max} - step_{R\text{-}functions}}{step_{\max}} \times 100\%. \tag{36}$$

5.2. The Messerschmitt–Bolkow–Blohm (MBB) beam example

The MBB beam example is another well-known benchmark example for examining the numerical performance of MMC-based TO approach [20,27,28]. Similar to the cantilever beam example, the design domain, geometric parameters and available solid material volume constraint as well as boundary conditions are all shown in Fig. 17. Only half of the design domain is taken into account due to the symmetry of the problem. The MBB beam problem is used to make a comparison over the ersatz material models used in the new formula of ITO-MMC proposed in Section 3 and the ersatz material models are presented Section 3.2. Then, it is shown an efficiency comparison between the IGA and FEM under the MMC-based TO framework. Recall that the TDF values of collocation points are calculated by Eq. (15) rather than max function in this example. The objective of half MBB beam problem is to find the optimal material distribution of structure which has the maximum stiffness under the available solid material constraint. The parameters of MMA are epsimin $= 10^{-7}$, raa0 $= 10^{-6}$, albefa $= 0.2$, asyinit $= 0.1$, asyincr $= 0.6$, asydecr $= 0.4$ for ITO-MMC in this subsection.

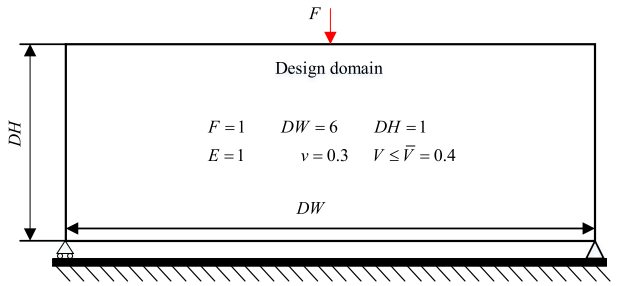

Fig. 17. Design domain of the MBB beam example.

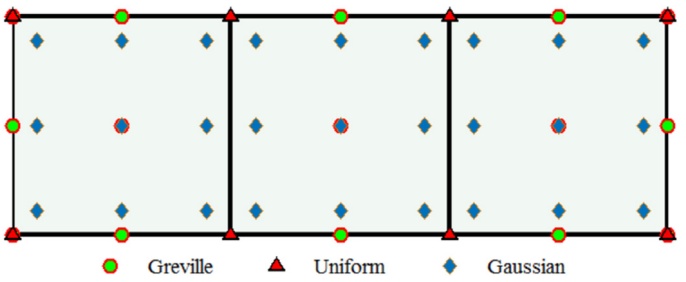

Fig. 18. The location of three different types collocation points are shown here for the ground structure discretized by IGA mesh with size of 3×1.

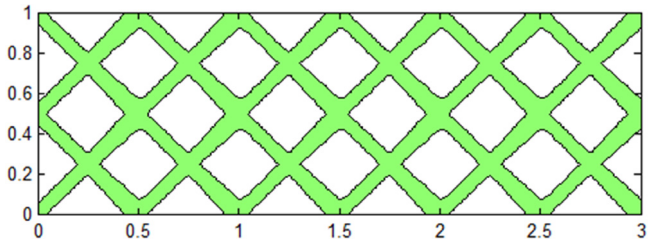

Fig. 19. The initial design of basic structural components.

5.2.1. Comparisons over three new ersatz material models

Three types of collocation points for the ersatz material models discussed in Section 3.2 are shown in Fig. 18 and the half MBB beam in Fig. 18 is discretized by quadratic 2D NURBS elements with mesh size 3×1 for the sake of illustration. The design domain of half MBB beam is discretized by quadratic 2D NURBS elements with mesh size 64×32 when it comes to carry out the new ITO-MMC proposed in this paper. The initial design of basic structural components shown in Fig. 19 is composed of 24 components which is similar to that in the previous example. Three new ersatz material models are used in the new ITO-MMC, respectively, and the max iteration step for new ITO-MMC is set to 700.

The final optimized and some intermediate structures of ITO-MMC for the three new ersatz material models cases are shown in Fig. 20. Meanwhile, the convergent curves of the values of objective function and volume fraction are given in Fig. 21. From the intermediate structures shown in Fig. 20 for each collocation scheme, we can easily find out that the three new ersatz material models are able to obtain an ideal structure, but only the structure produced by the ersatz material model based on Greville abscissae collocation scheme can meet the optimization criterion. Besides, a conclusion can be concluded from Fig. 21 that ersatz material model based on Greville abscissae collocation scheme has the highest stability compared to the other two models. Therefore, from the point of both convergence and stability, the ersatz material model based on Greville abscissae collocation scheme is the optimal choice to establish the ersatz material model used in the new ITO-MMC.

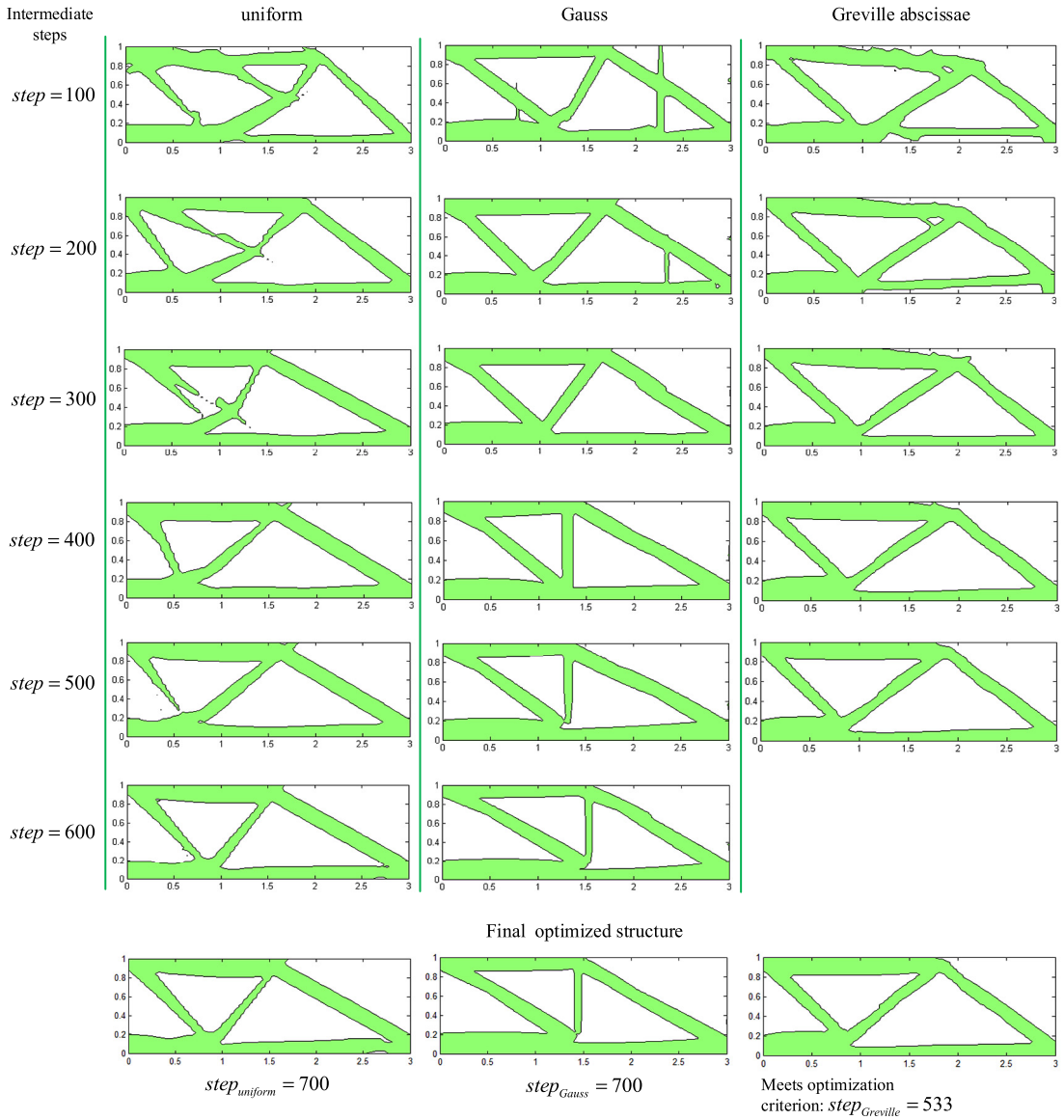

Fig. 20. The intermediate and final optimized structures: (a) left for new ersatz material model based on uniform collocation scheme; (b) middle for new ersatz material model based on Gauss collocation scheme; (c) right for new ersatz material model based on Greville abscissae collocation scheme.

5.2.2. IGA versus FEM

The high efficiency of high-order elements is one of the biggest advantages of IGA compared to conventional FEM. It is easily known from Fig. 22 that the number of degree of freedoms (DOFs) of IGA is much less than that of FEM. When the number of elements ($e_1 \times e_2$) is known, the DOFs of IGA (N_{IGA}) and the FEM (N_{FEM}) using quadratic elements are formulated as Eqs. (37) and (38), respectively. Therefore, the computation efficiency of IGA exceeds that of FEM with the same order of elements. For sake of simplicity, we only compare the efficiency of quadratic order elements between IGA and FEM under the framework of MMC-based TO. The definition of the ersatz material model from corresponding points is one of the key ingredients of MMC-based TO. The ersatz material model for Lagrange quadratic element used in FEM can be easily extended from that used in the conventional MMC-based TO [27] and the ersatz material model used in the new ITO-MMC is the ersatz material model based on Greville abscissae in terms

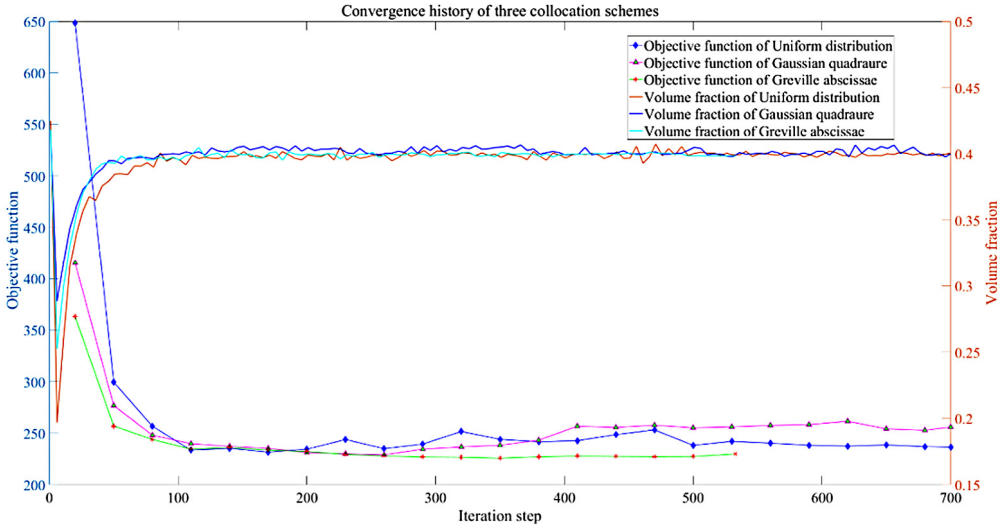

Fig. 21. Convergence history of three new ersatz material models based on the corresponding collocation schemes.

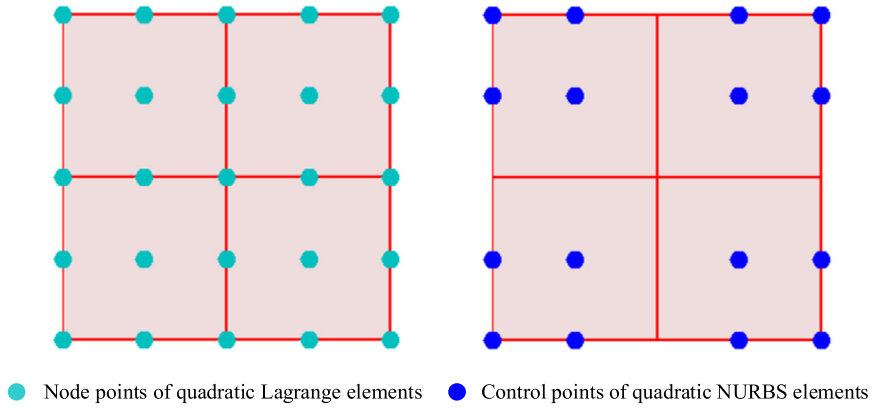

Fig. 22. An illustrative comparison of DOFs between FEM and IGA.

of the convergence and stability which have been demonstrated by the numerical result shown in Section 5.2.1. The design domain illustrated of half MBB beam as depicted in Fig. 17 is approximated by meshes with size of 50×25, 60×30, 70×35, 80×40, 90×45 and 100×50, where quadratic IGA element and Lagrange quadratic FEM element are used. The initial design of basic structural components used here is shown in Fig. 23. Moreover, the parameters of MMA used in this subsection are epsimin $= 10^{-10}$, raa0 $= 0.01$, albefa $= 0.4$, asyinit $= 0.1$, asyincr $= 0.8$, asydecr $= 0.6$ for MMC-based TO using Lagrange quadratic FEM element.

$$N_{IGA} = 2(e_1 + 2)(e_2 + 2) \tag{37}$$

$$N_{FEM} = 2(2e_1 + 1)(2e_2 + 1). \tag{38}$$

The computational time of each iteration step are listed in Table 2 and the curve of speedups versus to mesh type is illustrated in Fig. 24. The speedup of IGA/FEM ranges from 2.20 to 2.99, demonstrating the high efficiency of IGA than FEM. From Fig. 24, we can find that the speedups $time_{step}^{FEM}/time_{step}^{IGA}$ is basically increasing when the number of elements is increased. Therefore, the replacement of FEM by IGA could lead to higher efficiency once the higher mesh resolution is used in discretizing the design domain.

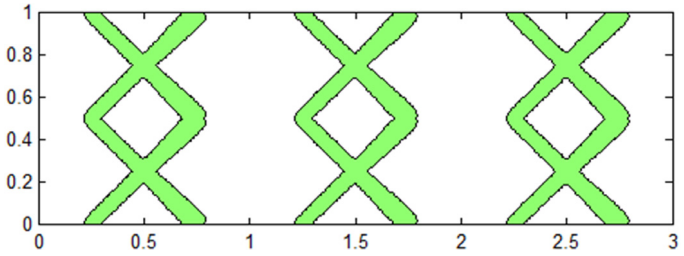

Fig. 23. Initial basic components design for all of the cases.

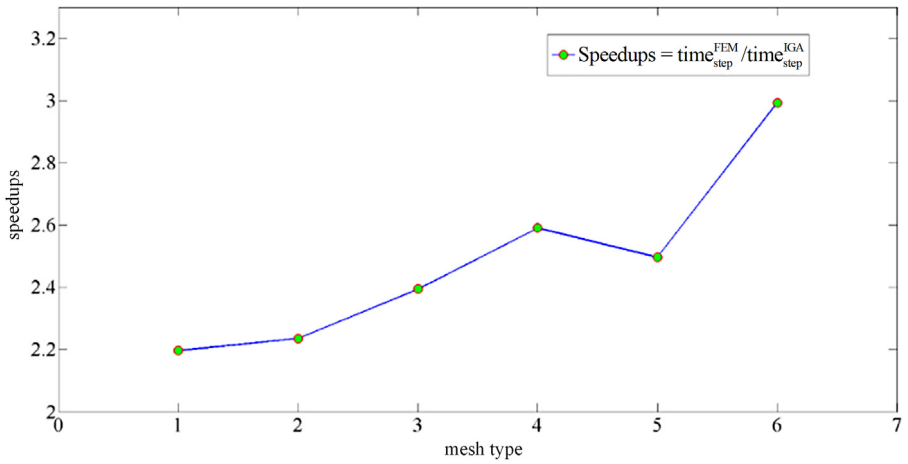

Fig. 24. The curve of speedups versus to mesh type.

Table 2
Efficiency comparison between IGA and the FEM by the computational time of one iteration.

Mesh type	Cases	N_{IGA}	N_{FEM}	IGA time: $time^{IGA}_{step}$ (s)	FEM time: $time^{FEM}_{step}$ (s)	Speedups(*IGA/FEM*) ($time^{FEM}_{step}/time^{IGA}_{step}$)
1	50 × 25	2 808	10 302	1.15	2.53	2.20
2	60 × 30	3 968	14 762	1.94	4.34	2.24
3	70 × 35	5 328	20 022	3.05	7.29	2.39
4	80 × 40	6 888	26 082	4.50	11.65	2.59
5	90 × 45	8 648	32 942	7.44	18.57	2.50
6	100 × 50	10 608	40 602	10.46	31.30	2.99

Fig. 25 shows the optimization results for different mesh size and different element type. An ideal optimal structure is obtained for almost all cases except for the cases where design domain discretized by 50 × 25 IGA elements and 80 × 40 FEM elements. The two failure cases may result from the inappropriate parameters of MMA and initial design of components. After changing the MMA parameters and initial design of components, ideal optimal structures can be obtained by MMC-based TO for the two failure cases, which are shown in Fig. 26. It is worth noting that the accuracy of IGA is higher than FEM in terms of the objection function values shown in Fig. 25, where all the objection function values obtained by IGA are smaller than those by FEM with the same mesh size.

5.3. Multiple load case

To verify the effectiveness of *R*-functions under the framework of ITO-MMC proposed in this paper, two and three dimensional short beams subjected to multiple load are taken into consideration. The maximum iteration step is set to

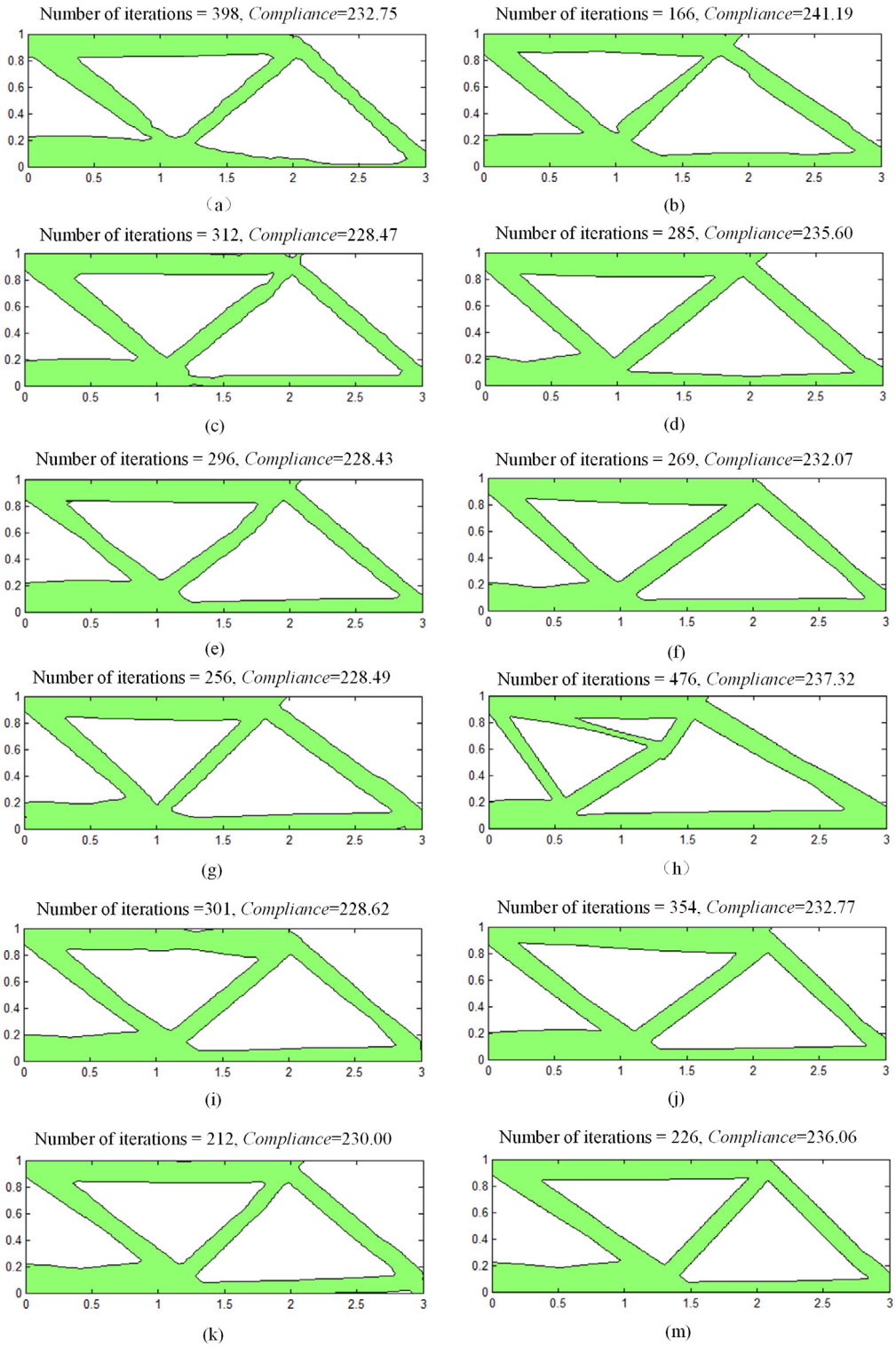

Fig. 25. The TO result of IGA and FEM with different meshes: (a) IGA with mesh 50 × 25, (b) FEM with mesh 50 × 25, (c) IGA with mesh 60 × 30, (d) FEM with mesh 60 × 30, (e) IGA with mesh 70 × 35, (f) FEM with mesh 70 × 35, (g) IGA with mesh 80 × 40, (h) FEM with mesh 80 × 40, (i) IGA with mesh 90 × 45, (j) FEM with mesh 90 × 45, (k) IGA with mesh 100 × 50, (m) FEM with mesh 100 × 50.

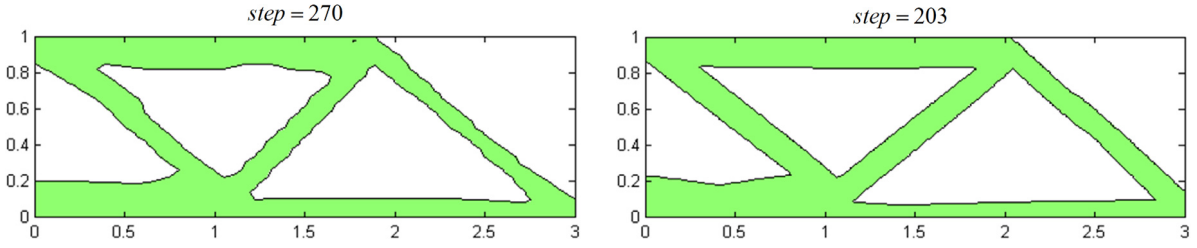

(a) NURBS elements with mesh size 50 × 25. (b) Lagrange elements with mesh size 80 × 40.

Fig. 26. The optimized structure for two failure cases in Fig. 25 after changing the parameters of MMA and the initial design of components.

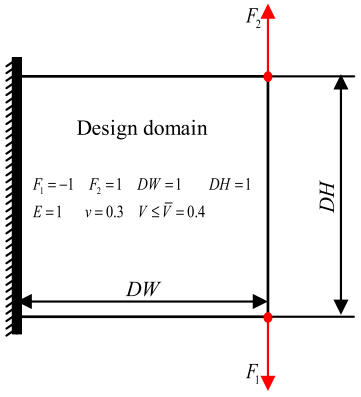

Fig. 27. Design domain for multi-load example.

400. In addition, the parameters of MMA are epsimin $= 10^{-10}$, raa0 $= 0.01$, albefa $= 0.3$, asyinit $= 0.1$, asyincr $= 0.4$, asydecr $= 0.2$ for ITO-MMC.

5.3.1. Two dimensional case

The problem setting of the two dimensional multiple load benchmark is illustrated in Fig. 27. And, the dimension of the multiple load benchmark is assumed to be 1×1. The left end of the multiple load beam is clamped, the right-up and right-bottom corner are prescribed with external load F_1 and F_2, respectively, and the volume ratio is set to 0.4 which is the same as that used in [65]. The new ITO-MMC and the new ersatz material model based on Greville abscissae are used in this benchmark according to the numerical result shown in Section 5.2.1. To discretize the multiple-load beam, quadratic NURBS elements with mesh size 40×40 are used. The initial designs of components are shown in Fig. 28 for cases where max function and R-functions are used for computing the TDF values.

Similar to the result in FEM, there is no distinguishable difference in the initial design of basic components for max function and R-functions cases in Fig. 28. Moreover, the difference in minimization compliance ($C_{R\text{-}functions} = 0.999C_{\max}$) and the final structure (shown in Figs. 29 and 30) are too small such that this difference can be ignored, which demonstrate that the R-function is an alternative choice for max function when calculating the TDF values. Whereas, according to the result of total iteration steps (to evaluate the convergence rate) at the top of Fig. 29, the difference in the convergence rate between max function case and R-functions case is distinct and the total iteration steps is reduced by 57 steps by replacing max function with R-functions. The improvement in convergence rate of R-functions is up to 16.9% (calculated by Eq. (36)), which shows that the R-functions outperforms max function under the IGA computation framework.

5.3.2. Three dimensional case

Fig. 31 makes an illustrative description of the three dimensional beam subjected to multiple load, which are fixed in the left face. The prescribed volume fraction is set to 0.4. Structural components forming the final optimized

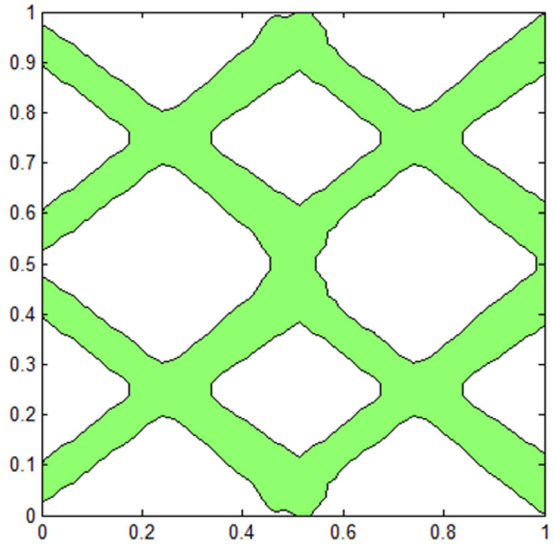

(a) Initial design of basic components with the use of max function.

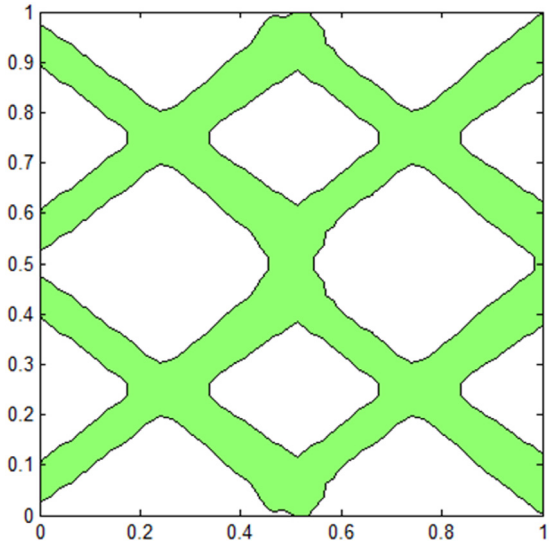

(b) Initial design of basic components with the use of R-functions.

Fig. 28. Initial design for basic components: (a) for max function and (b) for R-functions.

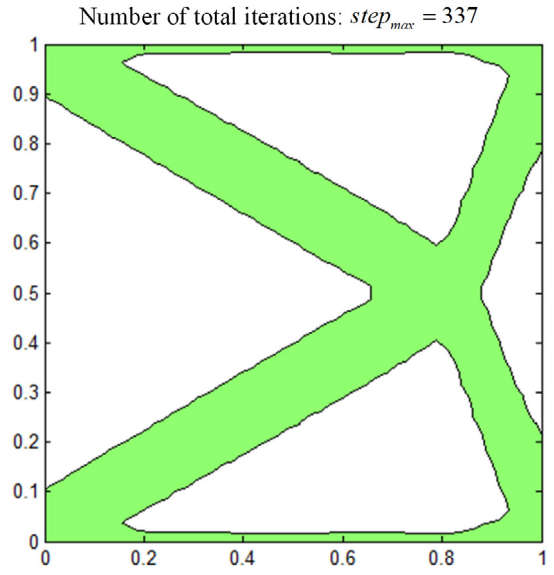

(a) The final optimal structure of the case of using max function and the compliance is $C = 60.47$.

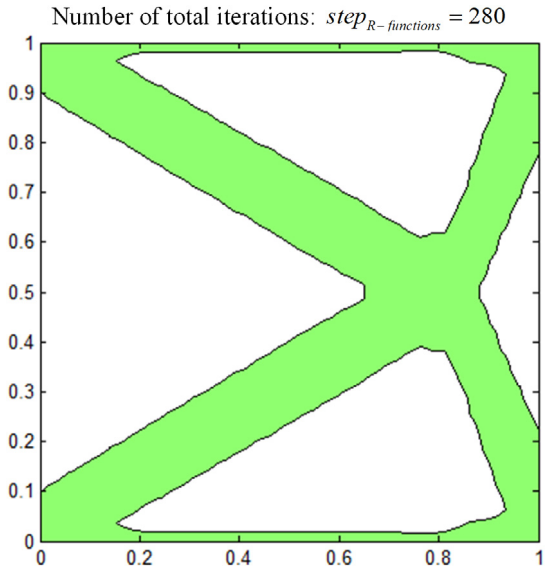

(b) The final optimal structure of the case of using R-function and the compliance is $C = 60.40$.

Fig. 29. The optimal structure of multiple load case for max function in the left and R-functions in the right.

topology structure are same to those used in the three dimensional cantilever case. Besides, the design domain is discretized into $40 \times 40 \times 4$ three dimensional quadratic NURBS elements. The components used here are similar to those used in Section 5.1.2, and the initial design of components are shown in Fig. 32.

With the aid of the ITO-MMC framework proposed in this paper, the final optimized three dimensional structures for max function and R-functions are presented in Fig. 33. According to the result shown in Fig. 33, it is known

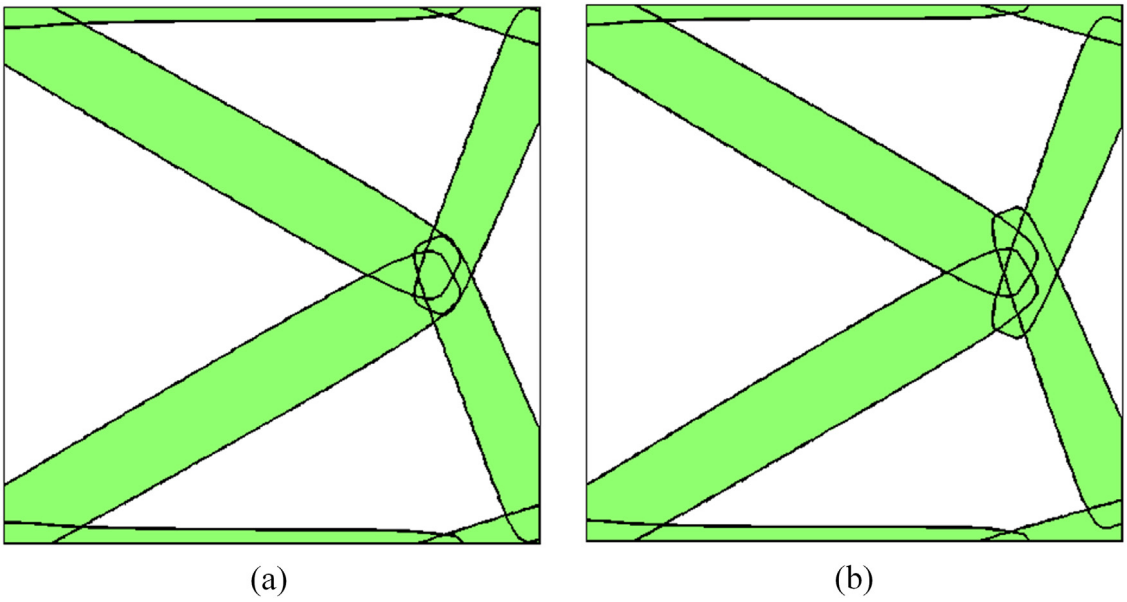

Fig. 30. The component plot: (a) for max function and (b) for R-functions.

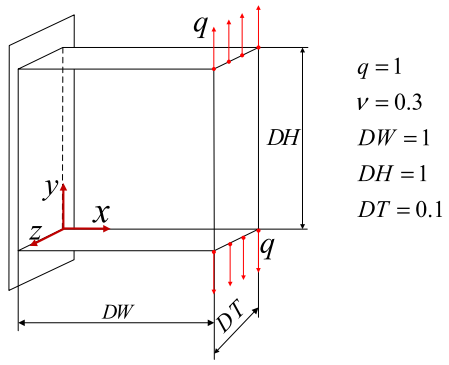

Fig. 31. The basic configuration of three dimensional beam subjected to multiple load.

that from the viewpoint of objective function, there is no difference between max function and R-functions under the framework of ITO-MMC($ratio = \frac{Compliance_{R\text{-}functions}}{Compliance_{\max}} = 0.994$).

However, compared to ITO-MMC using max function, the iteration step of ITO-MMC using R-functions is reduced by 89 steps, and the convergent rate is improved by 22.3% (calculated by Eq. (36)). It is concluded that R-functions outperforms max function in three dimensional ITO-MMC as well.

6. Conclusions

In this work, we have proposed a general and new formula of ITO-MMC based on R-functions and collocation points. It has been shown that the C^1 continuity provided by R-functions helps to accelerate the convergence rate of both conventional MMC-based TO and the new ITO-MMC. With the use of R-functions, the improvement in the convergence rate for both conventional MMC-based TO and the new ITO-MMC is in the range of 17%–60%, whilst there is no big difference in the final objective functional for the numerical examples. Therefore, the conventional MMC-based TO and ITO-MMC process based on R-functions can obtain a significant improvement in convergence rate (especially for three dimensional cases) and preserve the structural performance. The high efficiency of the

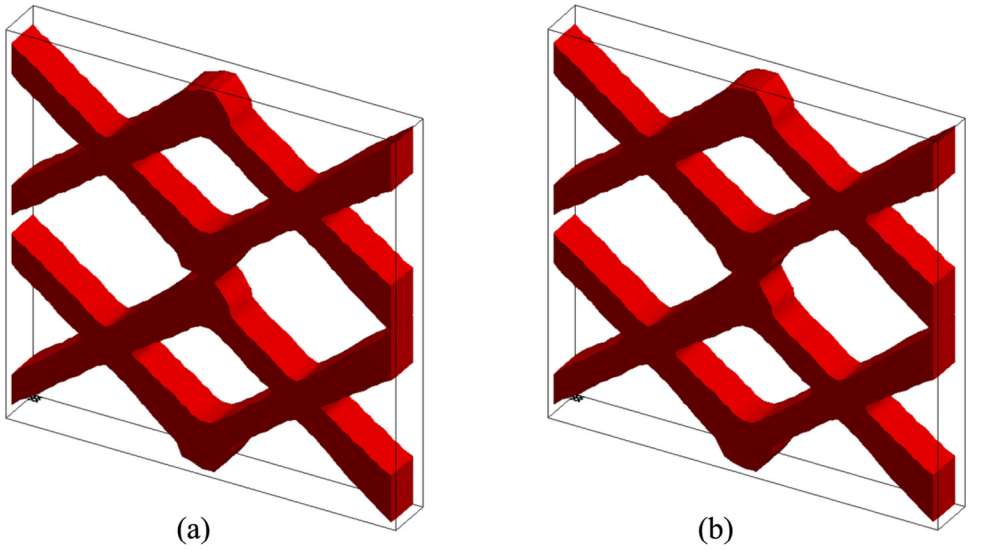

Fig. 32. The initial design of components: (a) for max function and (b) for R-functions.

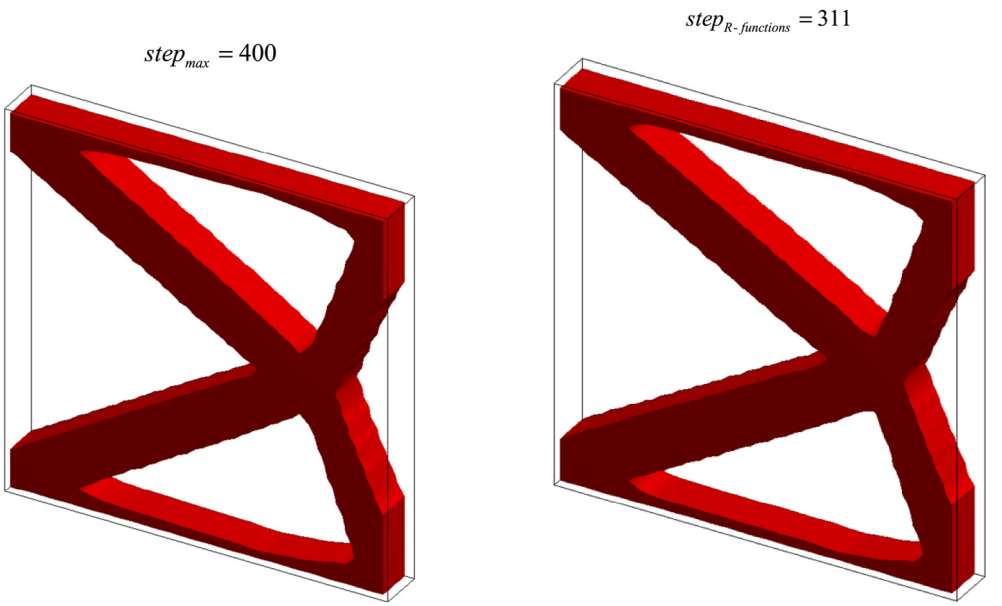

(a) $Compliance_{max} = 9390$. (b) $Compliance_{R\text{-}functions} = 9337$.

Fig. 33. The final structure optimized by ITO-MMC using max function is shown in (a), and the one optimized by ITO-MMC using R-functions is presented in (b).

proposed TDF calculation method based on R-functions results in a lower overall computational expense that enable larger problems to be solved at the same computational cost. Furthermore, the computational accuracy is improved by IGA to obtain a more accurate objective function.

It has been shown in the half MBB beam numerical test that the proposed ersatz material models based on uniform, Gauss and Greville abscissae collocation schemes of IGA are appropriate to define the constitutive behavior for the new ITO-MMC. From the view of both convergence and stability, the ersatz material model based on Greville

abscissae collocation scheme outperforms the other two ersatz material models. Therefore, the ersatz material model based on Greville abscissae collocation scheme is the optimal choice for defining the constitutive behavior of the new ITO-MMC proposed in this paper. By comparing the computational efficiency of IGA and FEM through the half MBB beam example with different mesh size, the speedups of IGA to FEM ranges from 2.20 to 2.99, which indicates the higher efficiency of IGA than that of conventional FEM.

Due to the heavier computational burden of MMC-based TO for solving the three-dimensional (3D) TO problems, the GPU parallel computing that has been successfully used in level-set based ITO [47] will be included to further accelerate the computational efficiency. In addition, the components used in MMC-based TO could also be made of two materials with distinct material properties. While clearly beyond the scope of the present work, such objectives could be carried out in future research works.

Acknowledgments

This work has been supported by both National Natural Science Foundation of China (51675197, 51705158). These supports are gratefully acknowledged.

References

[1] M.P. Bendsøe, N. Kikuchi, Generating optimal topologies in structural design using a homogenization method, Comput. Methods Appl. Mech. Engrg. 71 (2) (1988) 197–224.
[2] M.P. Bendsøe, Optimal shape design as a material distribution problem, Struct. Optim. 1 (4) (1989) 193–202.
[3] M. Zhou, G.I.N. Rozvany, The COC algorithm, Part II: Topological, geometrical and generalized shape optimization, Comput. Methods Appl. Mech. Engrg. 89 (1–3) (1991) 309–336.
[4] G. Allaire, F. Jouve, A.M. Toader, Structural optimization using sensitivity analysis and a level-set method, J. Comput. Phys. 194 (1) (2004) 363–393.
[5] Y. Mei, X. Wang, A level set method for structural topology optimization and its applications, Comput. Methods Appl. Mech. Engrg. 35 (7) (2004) 415–441.
[6] Q. Xia, M.Y. Wang, T. Shi, A level set method for shape and topology optimization of both structure and support of continuum structures, Comput. Methods Appl. Mech. Engrg. 272 (11) (2014) 340–353.
[7] Q. Xia, M.Y. Wang, T. Shi, Topology optimization with pressure load through a level set method, Comput. Methods Appl. Mech. Engrg. 283 (2015) 177–195.
[8] T. Liu, B. Li, S. Wang, L. Gao, Eigenvalue topology optimization of structures using a parameterized level set method, Struct. Multidiscip. Optim. 50 (4) (2014) 573–591.
[9] X. Qian, Full analytical sensitivities in NURBS based isogeometric shape optimization, Comput. Methods Appl. Mech. Engrg. 199 (29) (2010) 2059–2071.
[10] Y.M. Xie, G.P. Steven, A simple evolutionary procedure for structural optimization, Comput. Struct. 49 (5) (1993) 885–896.
[11] K. Maute, M. Allen, Conceptual design of aeroelastic structures by topology optimization, Struct. Multidiscip. Optim. 27 (1–2) (2004) 27–42.
[12] B. Stanford, P. Ifju, Aeroelastic topology optimization of membrane structures for micro air vehicles, Struct. Multidiscip. Optim. 38 (3) (2009) 301–316.
[13] J.-H. Zhu, W.-H. Zhang, L. Xia, Topology Optimization in Aircraft and Aerospace Structures Design, Arch. Comput. Methods Eng. 23 (4) (2016) 595–622.
[14] M. Langelaar, Topology optimization of 3D self-supporting structures for additive manufacturing, Addit. Manuf. 12 (2016) 60–70.
[15] T. Zegard, G.H. Paulino, Bridging topology optimization and additive manufacturing, Struct. Multidiscip. Optim. 53 (1) (2016) 175–192.
[16] X. Guo, J. Zhou, W. Zhang, Z. Du, C. Liu, Y. Liu, Self-supporting structure design in additive manufacturing through explicit topology optimization, Comput. Methods Appl. Mech. Engrg. 323 (2017) 27–63.
[17] Y.F. Li, X. Huang, F. Meng, S. Zhou, Evolutionary topological design for phononic band gap crystals, Struct. Multidiscip. Optim. 54 (3) (2016) 1–23.
[18] Y.F. Li, X. Huang, S. Zhou, Topological Design of Cellular Phononic Band Gap Crystals, Materials 9 (3) (2016) 186–208.
[19] N. Aage, E. Andreassen, B.S. Lazarov, O. Sigmund, Giga-voxel computational morphogenesis for structural design, Nature 550 (7674) (2017) 84–86.
[20] X. Guo, Doing topology optimization explicitly and geometrically—a new moving morphable components based framework, Frontiers Appl. Mech. 81 (8) (2014) 081009.
[21] W. Zhang, D. Li, J. Zhang, X. Guo, Minimum length scale control in structural topology optimization based on the Moving Morphable Components (MMC) approach, Comput. Methods Appl. Mech. Engrg. 311 (2016) 327–355.
[22] V.N. Hoang, G.W. Jang, Topology optimization using moving morphable bars for versatile thickness control, Comput. Methods Appl. Mech. Engrg. 317 (2017) 153–173.
[23] W. Zhang, J. Zhou, Y. Zhu, X. Guo, Structural complexity control in topology optimization via moving morphable component (MMC) approach, Struct. Multidiscip. Optim. 56 (3) (2017) 535–552.
[24] W. Zhang, W. Yang, J. Zhou, D. Li, X. Guo, Structural topology optimization through explicit boundary evolution, J. Appl. Mech. 84 (1) (2017).

[25] W. Zhang, J. Chen, X. Zhu, J. Zhou, D. Xue, X. Lei, X. Guo, Explicit three dimensional topology optimization via Moving Morphable Void (MMV) approach, Comput. Methods Appl. Mech. Engrg. 322 (2017) 590–614.
[26] X. Guo, W. Zhang, J. Zhang, J. Yuan, Explicit structural topology optimization based on moving morphable components (MMC) with curved skeletons, Comput. Methods Appl. Mech. Engrg. 310 (2016) 711–748.
[27] W. Zhang, J. Yuan, J. Zhang, X. Guo, A new topology optimization approach based on Moving Morphable Components (MMC) and the ersatz material model, Struct. Multidiscip. Optim. 53 (6) (2016) 1243–1260.
[28] W. Hou, Y. Gai, X. Zhu, X. Wang, C. Zhao, L. Xu, K. Jiang, P. Hu, Explicit isogeometric topology optimization using moving morphable components, Comput. Methods Appl. Mech. Engrg. 326 (2017) 694–712.
[29] Y. Wang, D.J. Benson, Isogeometric analysis for parameterized LSM-based structural topology optimization, Comput. Mech. 57 (1) (2016) 19–35.
[30] O. Sigmund, J. Petersson, Numerical instabilities in topology optimization: A survey on procedures dealing with checkerboards, mesh-dependencies and local minima, Struct. Optim. 16 (1) (1998) 68–75.
[31] T.J.R. Hughes, J.A. Cottrell, Y. Bazilevs, Isogeometric analysis: CAD, finite elements, NURBS, exact geometry and mesh refinement, Comput. Methods Appl. Mech. Engrg. 194 (39–41) (2005) 4135–4195.
[32] B. Marussig, T.J.R. Hughes, A Review of Trimming in Isogeometric Analysis: Challenges, Data Exchange and Simulation Aspects, Arch. Comput. Methods Eng. (8) (2017) 1–69.
[33] Y. Bazilevs, V.M. Calo, J.A. Cottrell, J.A. Evans, T.J.R. Hughes, S. Lipton, M.A. Scott, T.W. Sederberg, Isogeometric analysis using T-splines, Comput. Methods Appl. Mech. Engrg. 199 (5–8) (2010) 229–263.
[34] Y. Zhang, W. Wang, T.J.R. Hughes, Solid T-spline construction from boundary representations for genus-zero geometry, Comput. Methods Appl. Mech. Engrg. 249–252 (2012) 185–197.
[35] A.V. Vuong, C. Giannelli, B. Jüttler, B. Simeon, A Hierarchical Approach to Adaptive Local Refinement in Isogeometric Analysis, Comput. Methods Appl. Mech. Engrg. 200 (49) (2012) 3554–3567.
[36] Z.J. Wu, Z.D. Huang, Q.H. Liu, B.Q. Zuo, A local solution approach for adaptive hierarchical refinement in isogeometric analysis, Comput. Methods Appl. Mech. Engrg. 283 (2014) 1467–1492.
[37] Y. Bazilevs, V.M. Calo, T.J.R. Hughes, Y. Zhang, Isogeometric fluid–structure interaction: theory, algorithms, and computations, Comput. Mech. 43 (1) (2008) 3–37.
[38] Y. Bazilevs, J.R. Gohean, T.J.R. Hughes, R.D. Moser, Y. Zhang, Patient-specific isogeometric fluid–structure interaction analysis of thoracic aortic blood flow due to implantation of the Jarvik 2000 left ventricular assist device, Comput. Methods Appl. Mech. Engrg. 198 (45–46) (2009) 3534–3550.
[39] D.J. Benson, Y. Bazilevs, M.C. Hsu, T.J.R. Hughes, Isogeometric shell analysis: The Reissner–Mindlin shell, Comput. Methods Appl. Mech. Engrg. 199 (5) (2010) 276–289.
[40] J. Kiendl, K.U. Bletzinger, J. Linhard, R. Wüchner, Isogeometric shell analysis with Kirchhoff–Love elements, Comput. Methods Appl. Mech. Engrg. 198 (49) (2009) 3902–3914.
[41] H. Liu, X. Zhu, D. Yang, Isogeometric method based in-plane and out-of-plane free vibration analysis for Timoshenko curved beams, Struct. Eng. Mech. 59 (3) (2016) 503–526.
[42] X. Wang, X. Zhu, P. Hu, Isogeometric finite element method for buckling analysis of generally laminated composite beams with different boundary conditions, Int. J. Mech. Sci. 104 (2015) 190–199.
[43] E.D. Luycker, D.J. Benson, T. Belytschko, Y. Bazilevs, M.C. Hsu, X-FEM in isogeometric analysis for linear fracture mechanics, Internat. J. Numer. Methods Engrg. 87 (6) (2011) 541–565.
[44] K. Li, X. Qian, Isogeometric analysis and shape optimization via boundary integral, Comput. Aided Des. 43 (11) (2011) 1427–1437.
[45] J.A. Cottrell, T.J.R. Hughes, Y. Bazilevs, Isogeometric Analysis: Toward Integration of CAD and FEA,N Vol. 141, Wiley & Sons, 2015, pp. 299–325 (5).
[46] Y. Wang, H. Xu, D. Pasini, Multiscale isogeometric topology optimization for lattice materials, Comput. Methods Appl. Mech. Engrg. 316 (2016) 568–585.
[47] Z. Xia, Y. Wang, Q. Wang, C. Mei, GPU parallel strategy for parameterized LSM-based topology optimization using isogeometric analysis, Struct. Multidiscip. Optim. 56 (2) (2017) 1–22.
[48] Y.D. Seo, H.J. Kim, S.K. Youn, Isogeometric topology optimization using trimmed spline surfaces, Comput. Methods Appl. Mech. Engrg. 199 (49–52) (2010) 3270–3296.
[49] L. Dedè, M.J. Borden, T.J.R. Hughes, Isogeometric Analysis for Topology Optimization with a Phase Field Model, Arch. Comput. Methods Eng. 19 (3) (2012) 427–465.
[50] A.V. Kumar, A. Parthasarathy, Topology optimization using B-spline finite elements, Struct. Multidiscip. Optim. 44 (4) (2011) 471–481.
[51] Y. Wang, D.J. Benson, Geometrically constrained isogeometric parameterized level-set based topology optimization via trimmed elements, Front. Mech. Eng. 11 (4) (2016) 1–16.
[52] Q.X. Lieu, J. Lee, A multi-resolution approach for multi-material topology optimization based on isogeometric analysis, Comput. Methods Appl. Mech. Engrg. 323 (2017) 272–302.
[53] Y.D. Fougerolle, A. Gribok, S. Foufou, F. Truchetet, M.A. Abidi, Boolean operations with implicit and parametric representation of primitives using R-functions, IEEE Trans. Vis. Comput. Graphics 11 (5) (2005) 529–539.
[54] V.L. Rvachev, Theory of R-Functions and Some Applications, Econometrica 36 (5) (1982) 35–38.
[55] W. Zhang, J. Song, J. Zhou, Z. Du, Y. Zhu, Z. Sun, X. Guo, Topology optimization with multiple materials via Moving Morphable Component (MMC) method, Internat. J. Numer. Methods Engrg. (2017).
[56] T. Liu, S. Wang, B. Li, L. Gao, A level-set-based topology and shape optimization method for continuum structure under geometric constraints, Struct. Multidiscip. Optim. 50 (2) (2014) 253–273.

[57] W. Zhang, D. Li, J. Zhou, Z. Du, B. Li, X. Guo, A Moving Morphable Void (MMV)-based explicit approach for topology optimization considering stress constraints, Comput. Methods Appl. Mech. Engrg. (2018).
[58] K. Svanberg, The method of moving asymptotes—a new method for structural optimization, Internat. J. Numer. Methods Engrg. 24 (2) (1987) 359–373.
[59] L. Piegl, W. Tiller, The NURBS Book, Springer Berlin Heidelberg, 1997.
[60] C.D. Boor, On calculating with B -splines, J. Approx. Theory 6 (1) (1972) 50–62.
[61] A. Balestrino, A. Caiti, E. Crisostomi, S. Grammatico, Stabilizability of linear differential inclusions via R-functions, IFAC Proc. Vol. 43 (14) (2010) 1092–1097.
[62] T.N.E. Greville, Introduction to spline functions, Theory and Applications of Spline Functions, 1969, pp. 1–35.
[63] G. Farin, Curves and Surfaces for Cagd, Morgan Kaufmann, 2001.
[64] O. Sigmund, A 99 line topology optimization code written in Matlab, Struct. Multidiscip. Optim. 21 (2) (2001) 120–127.
[65] E. Andreassen, A. Clausen, M. Schevenels, B.S. Lazarov, O. Sigmund, Efficient topology optimization in MATLAB using 88 lines of code, Struct. Multidiscip. Optim. 43 (1) (2011) 1–16.
[66] K. Liu, A. Tovar, An efficient 3D topology optimization code written in Matlab, Struct. Multidiscip. Optim. 50 (6) (2014) 1175–1196.